

Arbeitsbericht NAB 12-50

**Geotechnical characterization of
core samples from the
geothermal well Schlattingen
SLA-1 by LMS/EPFL**

November 2012

A. Ferrari, V. Favero, D. Manca and L. Laloui

Laboratory for Soil Mechanics (LMS)
Swiss Federal Institute of
Technology, Lausanne (EPFL)

Nationale Genossenschaft
für die Lagerung
radioaktiver Abfälle

Hardstrasse 73
CH-5430 Wettingen
Telefon 056-437 11 11

www.nagra.ch

Arbeitsbericht NAB 12-50

Geotechnical characterization of core samples from the geothermal well Schlattingen SLA-1 by LMS/EPFL

November 2012

A. Ferrari, V. Favero, D. Manca and L. Laloui

Laboratory for Soil Mechanics (LMS)
Swiss Federal Institute of
Technology, Lausanne (EPFL)

KEYWORDS

Schlattingen, geotechnical characterization, host rock,
Opalinus Clay, 'Brauner Dogger', Effingen, Member,
retention behaviour, HM deformation behaviour,
swelling behaviour

Nationale Genossenschaft
für die Lagerung
radioaktiver Abfälle

Hardstrasse 73
CH-5430 Wettingen
Telefon 056-437 11 11

www.nagra.ch

Nagra Working Reports concern work in progress that may have had limited review. They are intended to provide rapid dissemination of information. The viewpoints presented and conclusions reached are those of the author(s) and do not necessarily represent those of Nagra.

"Copyright © 2012 by Nagra, Wettingen (Switzerland) / All rights reserved.

All parts of this work are protected by copyright. Any utilisation outwith the remit of the copyright law is unlawful and liable to prosecution. This applies in particular to translations, storage and processing in electronic systems and programs, microfilms, reproductions, etc."

Inhaltsverzeichnis

Inhaltsverzeichnis.....	I
Tabellenverzeichnis.....	II
Figurenverzeichnis	III
1 Introduction	1
1.1 Background and scope	1
1.2 The geothermal well Schlattingen-1	1
1.3 Report organisation.....	3
2 Laboratory program	5
3 Identification of the cores.....	9
3.1 Geotechnical characterization – methods and results	9
3.2 Pore size distribution – methods and results.....	15
4 Water-retention behaviour	21
4.1 Methodologies	21
4.1.1 Determination of the retention curves with investigation of the volumetric behaviour	22
4.1.2 Determination of the retention curves with progressive paths.....	25
4.1.3 Summary of the applied procedures for the determination of the retention properties of the tested cores	26
4.2 Results	26
4.2.1 Water retention curves with investigation of the volumetric behaviour	26
4.2.2 Water retention curves – progressive paths	31
5 Hydro-mechanical tests.....	37
5.1 Sample preparation procedure	37
5.2 Swelling tests	37
5.3 High-pressure oedometric tests.....	44
6 Conclusions.....	61
7 References.....	65
Appendix A – Structure of the electronic data base.....	67
Appendix B – Mineralogical Analyses of the Core samples by Professor Martin Mazurek / University of Berne	69

Tabellenverzeichnis

Tab. 1-1:	Important technical borehole information about the geothermal well Schlattingen-1.....	2
Tab. 2-1:	Description of the delivered cores.....	5
Tab. 2-2:	Complete list of tests.....	6
Tab. 2-3:	Composition of the artificial pore water (Traber, 2011).....	6
Tab. 3-1:	Results of the geotechnical characterization of the cores.....	10
Tab. 3-2:	Classification of the delivered cores according to the SN 670 004-2a.....	11
Tab. 3-3:	Properties of the samples used for the MIP tests before and after the freeze-drying (F-D).....	17
Tab. 3-4:	Summary of the results of MIP tests.....	17
Tab. 4-1:	Initial suction values.....	22
Tab. 4-2:	Method for the determination of the retention curve and paths followed for each core (PR: psychrometric readings; FDT: Fluid displacement technique).	26
Tab. 4-3:	Fitting parameters for the evolution of the void ratio with the total suction.	29
Tab. 4-4:	Curve fitting parameters for the Van Genuchten equation for samples BD-6, BD-18, BD-12, OPA3.	29
Tab. 4-5:	Curve fitting parameters for the Van Genuchten equation for samples BD-7, BD-30, BD-18, OPA-6, OPA-18, OPA-20.....	32
Tab. 5-1:	Performed swelling tests and initial properties of the samples.....	40
Tab. 5-2:	Swelling Pressure of the tested samples.....	43
Tab. 5-3:	Initial characteristics of the specimens tested in the high-pressure oedometric cell.....	46
Tab. 5-4:	Measured values of the swelling pressure in the high pressure oedometer tests. Swelling pressures were determined in the initial phase of sample saturation by applying of a low water pressure of about 50 kPa.....	46
Tab. 5-5:	Results of the high pressure oedometer tests: preconsolidation pressure, coefficient of compressibility and swelling coefficients for all the tested samples.....	53

Figurenverzeichnis

Fig. 1-1: Topographic map, displaying the location of the geothermal well Schlattingen-1 (SLA -1).....	1
Fig. 1-2: Stratigraphy of the geothermal well Schlattingen-1 (SLA -1) after Albert et al. (2012).....	3
Fig. 2-1: Photo documentation of the drillcore sections showing the position of the delivered cores.	7
Fig. 3-1: Plasticity chart (after SN 670 008a).....	11
Fig. 3-2: Grain size distributions of the BD cores.....	12
Fig. 3-3: Grain size distributions of the OPA cores.	13
Fig. 3-4: Grain size distributions of the EFM core.....	14
Fig. 3-5: Summary of the grain size distributions of the tested cores.	15
Fig. 3-6: Shale specimens for the MIP test (a), freeze-drying device (b) and dilatometer used for the analysis (c).....	16
Fig. 3-7: Cumulative intruded void ratio and (weighed) pore size distribution for the sample BD-6.....	17
Fig. 3-8: Cumulative intruded void ratio and pore size distribution for the sample BD-16.	18
Fig. 3-9: Cumulative intruded void ratio and pore size distribution for the sample BD-7.	18
Fig. 3-10: Cumulative intruded void ratio and pore size distribution for the sample BD-30.	18
Fig. 3-11: Cumulative intruded void ratio and pore size distribution for the sample OPA-3.....	19
Fig. 3-12: Cumulative intruded void ratio and pore size distribution for the sample EFM-1.....	19
Fig. 3-13: Summary of the pore size distributions for all tested samples.....	19
Fig. 4-1: Chilled-mirror dew point psychrometer.	21
Fig. 4-2: Division of the slice in five parts.	23
Fig. 4-3: Schematic representation of the system used to wet the samples.....	24
Fig. 4-4: Specimen preparation for the wetting path.....	24
Fig. 4-5: Phases of the FDT for sample volume measurement.	25
Fig. 4-6: Void ratio versus total suction for the cores from the 'Brown Dogger' formation.	27
Fig. 4-7: Void ratio versus total suction for the cores from the Opalinus Clay formation.	28
Fig. 4-8: Total suction versus water content and degree of saturation for the core BD-6.	29

Fig. 4-9:	Total suction versus water content and degree of saturation for the core BD-18.	30
Fig. 4-10:	Total suction versus water content and degree of saturation for the core BD-12.	30
Fig. 4-11:	Total suction versus water content and degree of saturation for the core OPA-3.	31
Fig. 4-12:	Total suction versus water content and degree of saturation for the core BD-7.	32
Fig. 4-13:	Total suction versus water content and degree of saturation for the core BD-18 (drying path).	33
Fig. 4-14:	Total suction versus water content and degree of saturation for the core BD-30 (wetting path).	33
Fig. 4-15:	Total suction versus water content and degree of saturation for the core OPA-6.	34
Fig. 4-16:	Total suction versus water content and degree of saturation for the core OPA-18.	34
Fig. 4-17:	Total suction versus water content and degree of saturation for the core OPA-20.	35
Fig. 4-18:	Total Suction versus water content for the core EFM-1.	35
Fig. 5-1:	Specimen preparation for swelling and oedometer tests.	37
Fig. 5-2:	Experimental setup for free swelling tests.	38
Fig. 5-3:	Experimental setup for constrained swelling tests.	39
Fig. 5-4:	Evolution of the swelling pressure and axial strain in the constrained swelling test on sample OPA-6.	40
Fig. 5-5:	Constrained swelling tests on sample BD-16.	41
Fig. 5-6:	Constrained swelling tests on sample BD-18.	41
Fig. 5-7:	Constrained swelling tests on sample OPA-2.	42
Fig. 5-8:	Constrained swelling tests on sample OPA-18.	42
Fig. 5-9:	Constrained swelling test on sample OPA-20.	43
Fig. 5-10:	Free swelling test on sample BD-18.	44
Fig. 5-11:	Free swelling test on sample OPA-20.	44
Fig. 5-12:	The high pressure oedometer cell at the LMS-EPFL.	45
Fig. 5-13:	Comparison of the values of swelling pressure obtained in the high pressure oedometer cell and with the constrained swelling tests.	47
Fig. 5-14:	Oedometer curve for the core BD-6.	48
Fig. 5-15:	Oedometer curve for the core BD-7.	48
Fig. 5-16:	Oedometer curve for the core BD-12.	49
Fig. 5-17:	Oedometer curve for the core BD-16.	49
Fig. 5-18:	Oedometer curve for the core OPA-2.	50

Fig. 5-19:	Oedometric curve for the core OPA-20.....	50
Fig. 5-20:	Oedometric curve for the core OPA-6.....	51
Fig. 5-21:	Oedometric curve for the core OPA-18.....	51
Fig. 5-22:	Swelling coefficients versus maximum attained vertical effective stress for the 'Brown Dogger' and for the Opalinus Clay cores.	52
Fig. 5-23:	Coefficients of compressibility for all the tested cores.....	52
Fig- 5-24:	Oedometric modulus and coefficient of consolidation versus vertical effective stress for core BD-6.	53
Fig- 5-25:	Oedometric modulus and coefficient of consolidation versus vertical effective stress for the core BD-7.	54
Fig. 5-26:	Oedometric modulus and coefficient of consolidation versus vertical effective stress for the core BD-12.	54
Fig. 5-27:	Oedometric modulus and coefficient of consolidation versus vertical effective stress for the core BD-16.	55
Fig. 5-28:	Oedometric modulus and coefficient of consolidation versus vertical effective stress for the core OPA-2.....	55
Fig. 5-29:	Oedometric modulus and coefficient of consolidation versus vertical effective stress for the core OPA-20.....	56
Fig. 5-30:	Oedometric modulus and coefficient of consolidation versus vertical effective stress for the core OPA-6.....	56
Fig. 5-31:	Oedometric modulus and coefficient of consolidation versus vertical effective stress for the core OPA-18.....	57
Fig. 5-32:	Oedometric modulus and coefficients of consolidation versus vertical effective stress for the 'Brown Dogger' cores.	57
Fig. 5-33:	Oedometric modulus and coefficients of consolidation versus vertical effective stress for the Opalinus Clay cores.....	58
Fig. 5-34:	Permeability versus vertical effective stress and permeability versus void ratio for the cores from the 'Brown Dogger' formation, as back-calculated from the analysis of the settlement versus time curves.	59
Fig. 5-35:	Permeability versus vertical effective stress and permeability versus void ratio for the cores from the Opalinus Clay formation, as back-calculated from the analysis of the settlement versus time curves.	59
Fig. 5-36:	Comparison of permeability versus vertical effective stress and permeability versus void ratio for the cores from the 'Brown Dogger' and Opalinus Clay formations.	60

1 Introduction

1.1 Background and scope

The Laboratory for Soil Mechanics (LMS) of the Swiss Federal Institute of Technology in Lausanne (EPFL) was requested by NAGRA to perform a geomechanical testing program on core samples extracted from a deep geothermal well near the village of Schlattingen in the Molasse Basin of Northern Switzerland. The laboratory studies are aimed at characterising three candidate host rock formations for the disposal of radioactive waste, namely the Effingen Member, the so-called 'Brown Dogger' (stratigraphic sequence of Callovian, Bathonian and Bajocian age) and the Opalinus Clay. The investigation programme comprises basic geotechnical identification tests, determination of the water retention behaviour and hydro-mechanical tests. The results of the laboratory investigations will feed in Nagra's data base on hydrogeological host rock properties. The electronic data base is enclosed in Appendix A. After completion of the geotechnical characterisation, a mineralogical analysis was performed on the left-overs of the tested core samples. The results of the mineralogical investigations are presented in appendix B.

1.2 The geothermal well Schlattingen-1

The geothermal well Schlattingen-1 (SLA-1) is located on the road between Basadingen, Schlattingen and Diessenhofen (Canton Thurgau) about 10 km south-east of the town Schaffhausen (approx. N 47°40'41.7", E 8°45'42"; 416.6 m asl) in the Northeastern part of the Swiss Molasse Basin (Figure 1-1). The borehole is intended to produce geothermal energy for an economical and CO₂-emmission-free operation of greenhouses. Therefore, during 2011, a first deep borehole Schlattingen-1 was drilled to use the ground water from aquifers in the Upper Muschelkalk and the transition Mesozoic / permo-carboniferous - crystalline rocks. The borehole reached a final depth of 1508 m, passed through the Quaternary, Tertiary, Jurassic and Triassic sediment sequence (with marls, silt-, sand-, and claystones, limestones) and finally encountered the crystalline basement (Albert et al. 2012).



Fig. 1-1: Topographic map, displaying the location of the geothermal well Schlattingen-1 (SLA -1).

The drilling of borehole Schlattingen-1 was accompanied by an extensive site characterization program, including lithostratigraphic and structural mapping of drillcores in the clay-rich Mesozoic sequences, geophysical logging, hydraulic packer testing, water sampling and hydraulic fracturing stress measurements. Focus of the investigations was on the geological and geotechnical characterisation of the candidate host rock formations, namely the Effingen Member, the so-called 'Brown Dogger' (stratigraphic sequence of Callovian, Bathonian and Bajocian age) and the Opalinus Clay. The stratigraphic profile of borehole Schlattingen-1 is shown in Figure 1-2, available technical borehole data are summarized in Table 1-1.

Tab. 1-1: Important technical borehole information about the geothermal well Schlattingen-1.

Geothermal Well Schlattingen-1 – SLA 1		
Location	Village of Schlattingen, around 10 km south-east of Schaffhausen	
Co-ordinates	N 47°40'41.7", E 8°45'42"	
Elevation	416.6 m asl	
Max. depth:	1508.0 bg	
Drilling techniques	Percussion drilling, cuttings:	0 - 725 m bg 989 - 1116 m bg 1185 - 1508 m bg
	Single barrel core drilling:	725 - 989 m bg 1116 - 1185 m bg
Investigation programme	Petrophysical logging:	GR, FEL, DIL, DLL, Gamma-Gamma, Neutron-Neutron, Sonic)
	Core mapping / structural logging:	ABF, ABI
	Packer Testing:	4 Tests
	Hydrofracturing:	15 Tests
	Porewater sampling:	4 Samples
	Mineralogical and geotechnical characterization of core samples	(> 50 samples tested)

Geothermal Well Schlattingen-1							
Stratigraphy	Depth	Lithology	Thickness [m]	Unit			
Quaternary	53		53	Quaternary			
NEOGENE	125		72	Upper Marine Molasse (OMM)			
				PALEOGENE	Oligocene	364	Lower Freshwater Molasse (USM)
Eocene	491		2				Bohnerz-Formation
JURASSIC	Malm		58	Plattenkalk			
				Kimmeridgian	643	94	Massenkalk/Quaderkalk
							674
				Oxfordian	720	46	Wohlgeschichtete Kalke
	733.1	Hornbuck-Schichten					
	Dogger		46.8	Effingen Beds			
				757.8	Birmenst. Sch., Glaukonit-Sandmergel		
				804.6	Anceps-O., Macroceph.-Sch., Varians-Sch., Parkinsoni-Württembergica-Sch., Subfurcata-Ool., Blagdeni-Sch., Humphriesi-Sch.		
				831.4	Wedelsandstein-Formation		
	Aalenian	949.7	118.3	Opalinus Clay			
Liassic	1003	53.3	Jurensis-Schichten – Psiloceras-Schichten				
TRIASSIC	Keuper		44	Knollenmergel, Stubensandstein-Fm., Bunte Mergel, Gansinger Dolomit, Schilfsandstein			
				1047	Gipskeuper		
				1112	Lettenkohle		
	Muschelkalk		33.3	Trigonodus-Dolomit			
				1145.3	Hauptmuschelkalk		
	Lower Buntsandstein		24.2	Dolomit der Anhydritgruppe			
				1169.5	Anhydritgruppe (Sulfatschichten)		
Middle		53	Wellengebirge				
			1223	Buntsandstein			
Permian		29	Rotliegendes				
			1251				
PALEOZOIC	Crystalline		10	Gneiss			
				1261			
Total depth			1508 m				

Fig. 1-2: Stratigraphy of the geothermal well Schlattingen-1 (SLA-1) after Albert et al. (2012).

1.3 Report organisation

This report summarizes the results of the experimental activities carried out in the laboratories of LMS/EPFL. The test program is first described in Section 2. Section 3 presents the results of the cores characterization in terms of index properties and pore size distribution. Section 4 describes the determination of the water retention curves. Mechanical tests are presented in Section 5.

2 Laboratory program

Eleven of a total of 12 cores from Schlattingen were delivered at the EPFL on 7 May 2011 while an additional core was delivered in March 2012. Table 2-1 reports the description of the cores as provided by Nagra; the "Nagra Code" is used in the following to identify the cores. Six cores belonged to the 'Brown Dogger' formation (BD) while 5 cores were from the Opalinus Clay formation (OPA); the last delivered core belonged to the Effingen Member (EFM). A photo documentation of the drillcore sections is reported in Figure 2-1.

Tab. 2-1: Description of the delivered cores.

Nagra Code	Depth	Lithology	Description (as reported on the tube)	Date	Length
BD-6	766.67 767.00	Clay to Argillaceous Marl	SLA 16 PEM	19.03.2011	33 cm
BD-16	769.55 769.85	Clay to Argillaceous Marl	Nagra PEM SLA 20	20.03.2011	28 cm
BD-18	774.95 775.16	Clay to Argillaceous Marl	OED SLA KM 21	20.03.2011	30 cm
BD-12	778.30 778.52	Argillaceous Marl	OED 19/Harz	21.03.2011	21 cm
BD-7	781.18 781.48	Calcareous Marl	PEM 19.15 Uhr	19.03.2011	30 cm
BD-30	807.14 807.44	Calcareous Marl	SLA PEM Nagra	23.03.2011	30 cm
OPA-3	837.44 837.66	Clay to Argillaceous Marlstone	NAGRA OED	11.04.2011	27 cm
OPA-2	837.98 838.25	Claystone	NAGRA OED	11.04.2011	22 cm
OPA-20	854.60 854.82	Claystone	NAGRA OED 1/1	18.04.2011	25 cm
OPA-6	882.20 882.50	Claystone with fine-sandy layers (ca. 1 mm)	NAGRA PEM	13.04.2011	22 cm
OPA-18	891.00 891.25	Claystone with sandy layers	NAGRA PEM	17.04.2011	30 cm
EFM-1	738.52 738.76	-	-	01.03.2012	24 cm

The first eleven cores were stored in black PVC tubes filled with a layer of resin and constrained with a metal frame. A photographic survey of the received cores is presented in the annex. All the cores appeared as undamaged and presented good storing condition. Core OPA-6 was reported to be kept in the borehole during ca. 3 hours because of tear-off; core BD-18 was resinated two times because the first layer did not harden. Cores OPA-3 and OPA-2 were reported to present Murchisonae oolith layers. The EFM core was wrapped in a plastic sleeve under vacuum.

The complete list of the performed tests is reported in Table 2-2. The analyses included the identification of the materials in terms of particle density, bulk density, water content, void ratio, degree of saturation, Atterberg limits and grain size distribution; the identification is completed by the determination of the pore size distribution for 6 cores by mercury intrusion porosimetry (MIP). The water retention behaviour is analysed for the majority of the cores. The hydro-mechanical behaviour is characterized in terms of swelling behaviour and oedometric response under high stress conditions. Synthetic pore water is used in the all the experiments with the aim to reproduce the composition of the in-situ water (Table 2-3). The osmotic suction of this synthetic pore water measured with the dew point meter was about 1 MPa.

Tab. 2-2: Complete list of tests.

Core	Identification	MIP	1D volumetric response	Swelling tests	Retention curves	Water permeability
EFM-1	x	1			1	
BD-6	x	1	1		1	1
BD-16	x	1	1	1		1
BD-18	x			2	1	
BD-12	x		1		1	1
BD-7	x	1	1		1	1
BD-30	x	1			1	
OPA-3	x	1			1	
OPA-2	x		1	1		1
OPA-20	x		1	2	1	1
OPA-6	x		1	1	1	1
OPA-18	x		1	1	1	1
TOT:	12	6	8	8	10	8

Tab. 2-3: Composition of the artificial pore water (Traber, 2011).

Cationic component	mmol/kg _{H2O}	mg/kg _{H2O}	Anionic component	mmol/kg _{H2O}	mg/kg _{H2O}
Na	163.8	3765.7	Cl	169.0	5672.5
K	2.551	99.75	SO ₄	24.00	2305.5
Ca	11.91	477.4	HCO ₃	0.5431	33.14
Mg	9.166	222.8			

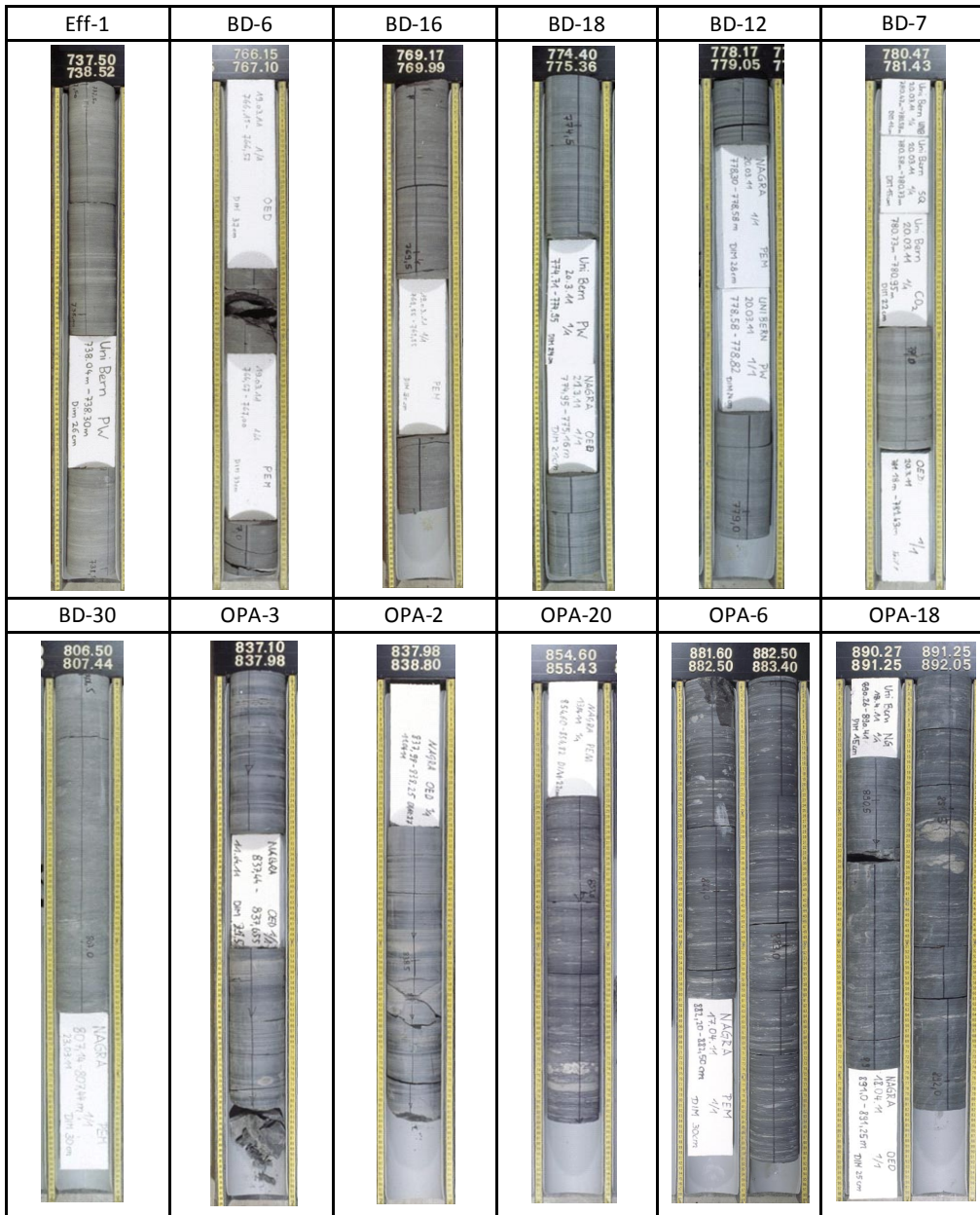


Fig. 2-1: Photo documentation of the drillcore sections showing the position of the delivered cores.

3 Identification of the cores

3.1 Geotechnical characterization – methods and results

The results of the geotechnical identification of the cores are summarised in Table 3-1, which reports:

- the particle density (ρ_s , ratio of the solid phase mass to the volume of the solid phase),
- the bulk density (ρ , ratio of the mass of the material to its total volume),
- the water content (w , ratio of the weight of the water to the weight of the solid phase),
- the void ratio (e , the ratio of the volume of pores to the volume of the solid phase),
- the degree of saturation (S_r , the ratio of the volume of water to the volume of pores),
- the Atterberg limits (liquid limit w_L ; plastic limit w_P , plasticity index PI),
- the grain size distribution, and
- the classification of the materials.

The particle density was measured following the ASTM D854-10 (Standard Test Methods for Specific Gravity of Soil Solids by Water Pycnometer; see www.astm.org) on material preliminarily crushed and passing a 4.75 mm sieve. Average values on two determinations are reported.

The bulk density was obtained by the water displacement method. Measurement were carried out on 3 cm high slices trimmed from the cores (sample weight of about 500g); two coats of melted paraffin were applied to the specimen with a brush; the waxed specimen was immersed in the water displacement apparatus and its volume was obtained by the weight of the overflowed water and considering the applied paraffin for which the density is known. After removing the paraffin wax, the water content was measured by oven-drying the slices at 105°C for 24 hours.

The void ratio and the degree of saturation were computed according to the following relationships:

$$e = \frac{\rho_s(1+w)}{\rho} - 1 \quad S_r = \frac{\rho_s W}{\rho_w e} \quad (3-1)$$

where ρ_w is the density of the water ($\rho_w = 1 \text{ Mg/m}^3$).

Atterberg limits were determined according to the SN 670 345a. The cores were classified according to the SN 670 004-2a. Results are depicted on the plasticity chart in Figure 3-1. Classification of the cores is reported in Table 3-2.

The grain size distribution was obtained by sedimentation analysis following the SN 670 816. In order to carry out the sedimentation analysis, the material was crushed initially by means of a grinder and the fraction passing a 0.5 mm sieve was selected. The crushed material was placed in distilled water along with a dispersing agent (tetra-sodium pyrophosphate) and shaken overnight. The effect of a longer shaking time has been taken into consideration and it has shown negligible effects on the final results of the tests. The obtained grain size distributions are reported in Figure 3-2 - Figure 3-4 for the three different tested materials. The figures show that the obtained curves are situated on the left of the maximum dimension of the selected material;

this observation confirms that the material does not present particles with a diameter larger than the maximum dimension of the crushed blocks; also it validates the procedure selected for the preparation of the sedimentation analysis.

Figure 3-5 presents a comparison of the gran size distributions of the 'Brown Dogger' and Opalinus Clay, showing a slightly greater percentage of fine material in the latter compared to the former one; in addition the grain size distribution of the EFM core is represented in the same graph showing a greater percentage of fine compared to the 'Brown Dogger' and Opalinus Clay formations.

Tab. 3-1: Results of the geotechnical characterization of the cores.

Core	ρ_s	ρ	w	e	S_r	w_L	w_P	PI	Grain size fract. (%)		
	(Mg/m ³)	(Mg/m ³)	(%)	(-)	(%)	(%)	(%)	(%)	sand	silt	clay
EFM-1	2.67	2.57	1.05	0.05	56	23	15	8	8	57	35
BD-6	2.75	2.56	2.7	0.10	72	25	22	3	27	55	18
BD-16	2.76	2.56	2.7	0.11	69	25	18	7	15	63	22
BD-18	2.74	2.55	3.2	0.11	81	25	19	6	19	61	20
BD-12	2.72	2.55	3.5	0.10	92	29	23	6	27	57	16
BD-7	2.70	2.52	4.4	0.12	100	33	21	12	23	51	26
BD-30	2.75	2.56	2.9	0.11	76	27	10	17	25	61	14
OPA-3	2.74	2.49	4.3	0.15	80	39	22	17	23	55	22
OPA-2	2.71	2.49	4.9	0.14	94	36	25	11	27	46	27
OPA-20	2.72	2.55	3.6	0.11	93	31	22	9	25	57	18
OPA-6	2.71	2.56	3.3	0.09	96	29	19	10	24	58	18
OPA-18	2.70	2.54	3.6	0.10	96	33	19	13	25	53	22

Tab. 3-2: Classification of the delivered cores according to the SN 670 004-2a.

Core	Grain size fract. (%)			Classif.	Description
	sand	silt	clay		
EFM-1	8	57	35	CL	Silty clay
BD-6	27	55	18	ML	Silt with sand
BD-16	15	63	22	CL-ML	Clayey silt with sand
BD-18	19	61	20	CL-ML	Clayey silt with sand
BD-12	27	57	16	CL-ML	Clayey silt with sand
BD-7	23	51	26	CM	Lean clay with sand
BD-30	25	61	14	CL	Silty clay with sand
OPA-3	23	55	22	CM	Lean clay with sand
OPA-2	27	46	27	ML	Silt with sand
OPA-20	25	57	18	CM	Lean clay with sand
OPA-6	24	58	18	CL	Silty clay with sand
OPA-18	25	53	22	CM	Lean clay with sand

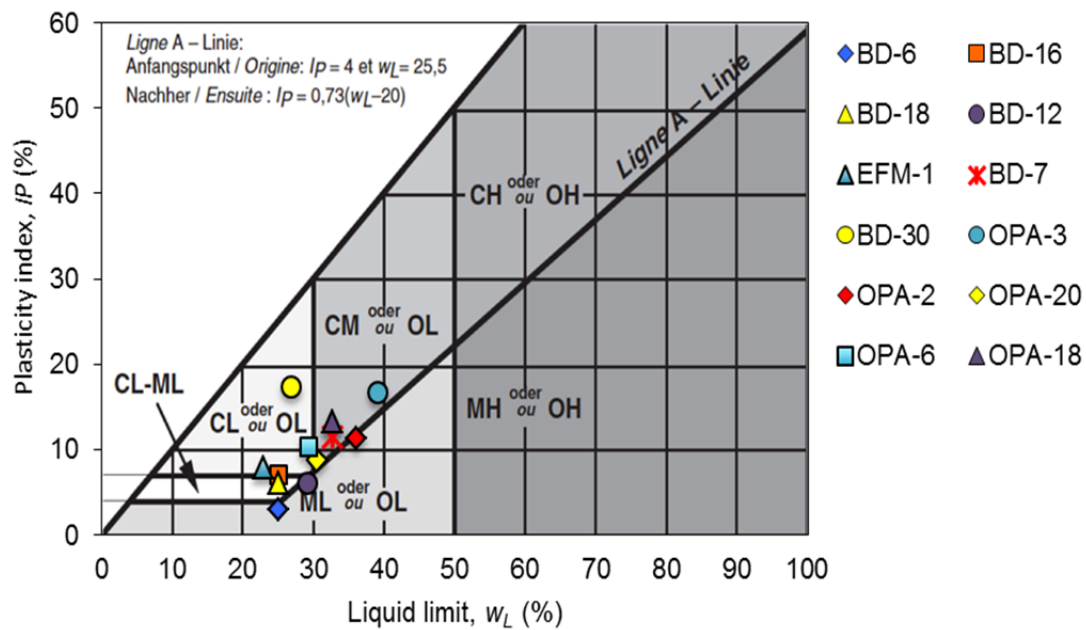


Fig. 3-1: Plasticity chart (after SN 670 008a).

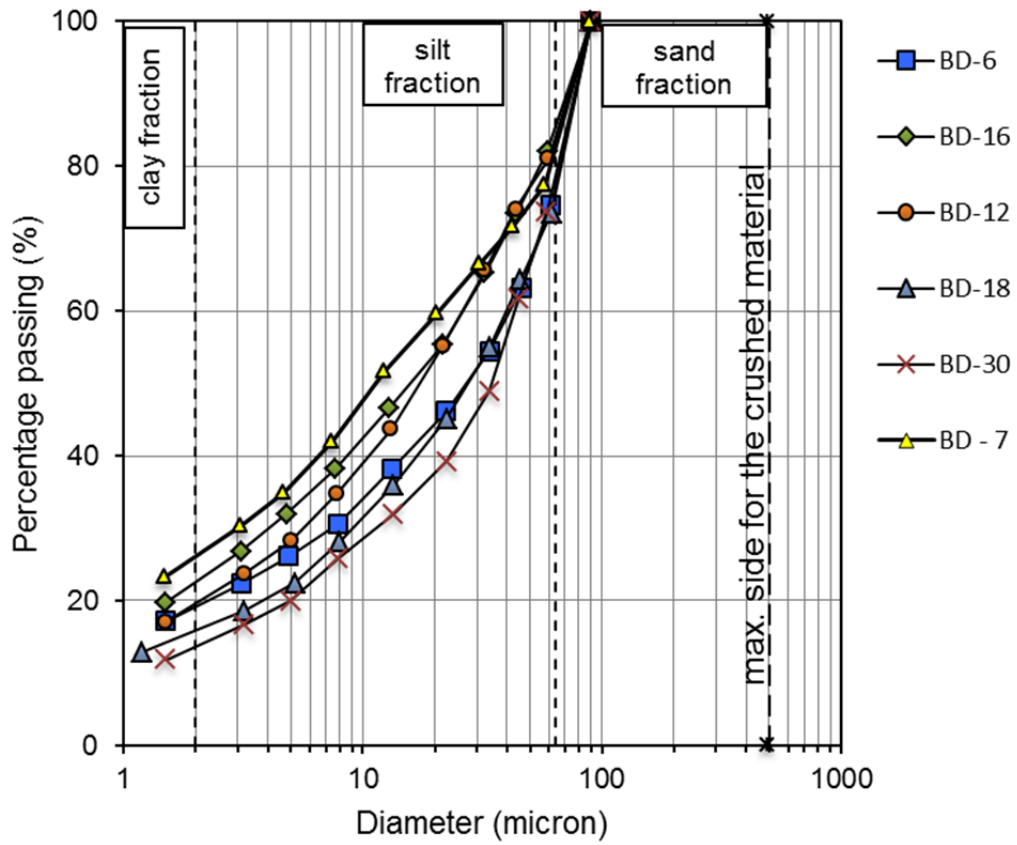


Fig. 3-2: Grain size distributions of the BD cores.

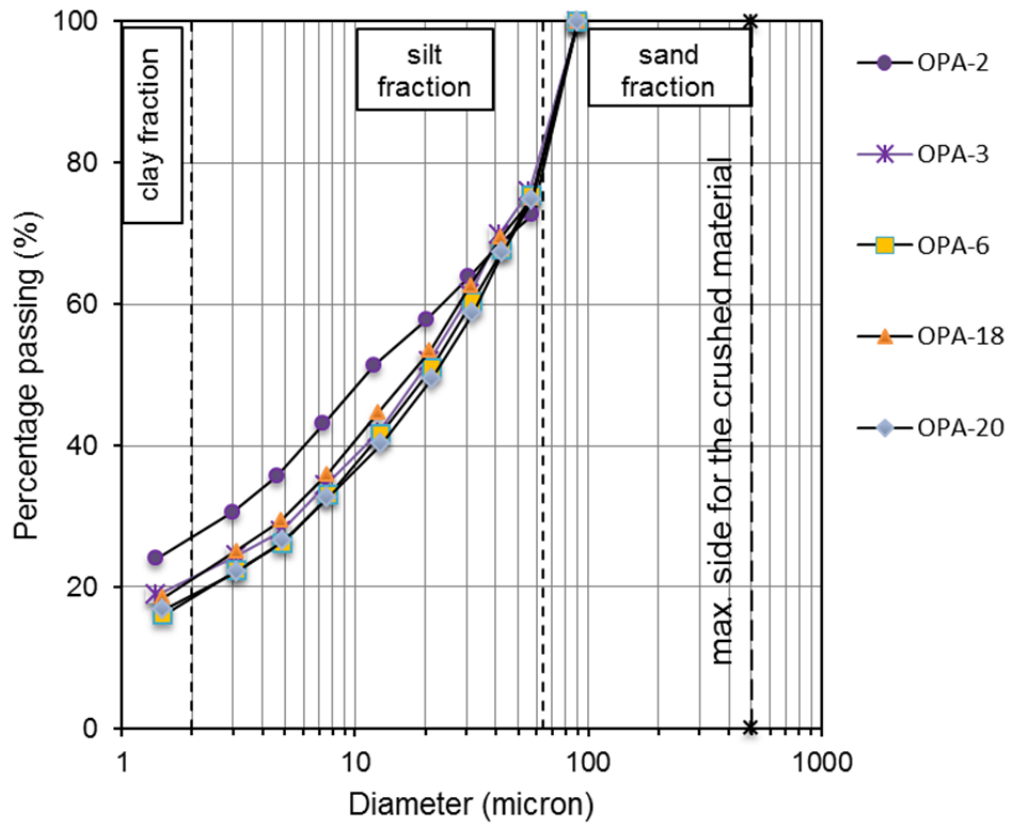


Fig. 3-3: Grain size distributions of the OPA cores.

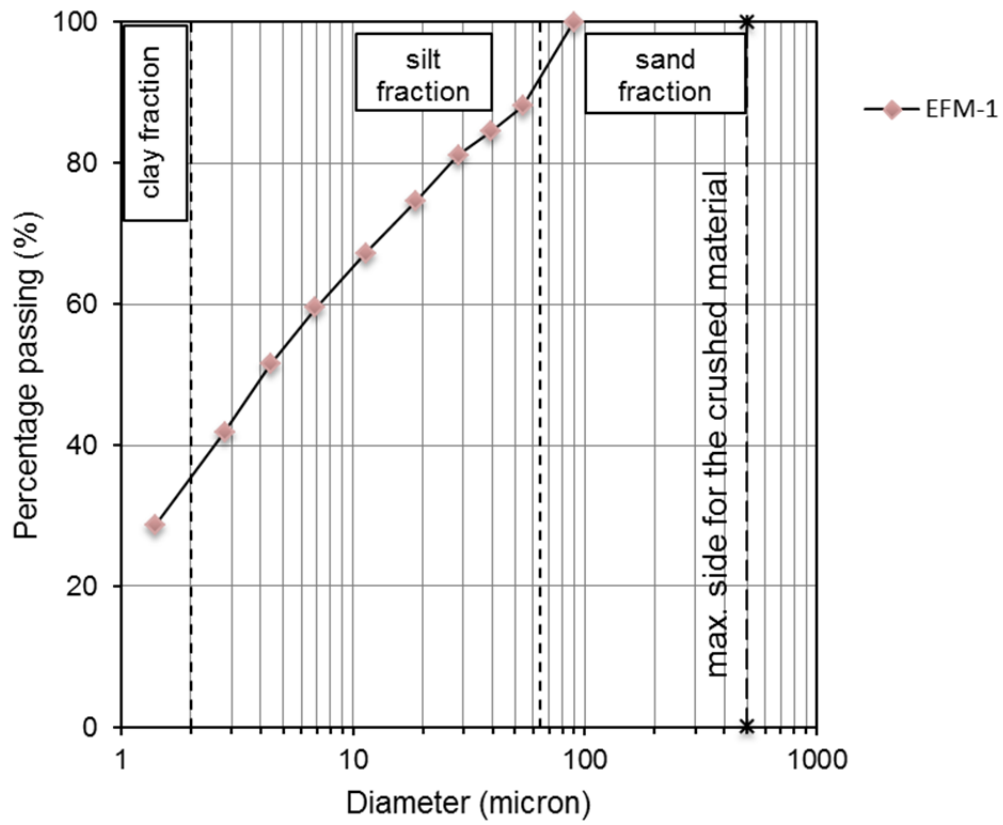


Fig. 3-4: Grain size distributions of the EFM core.

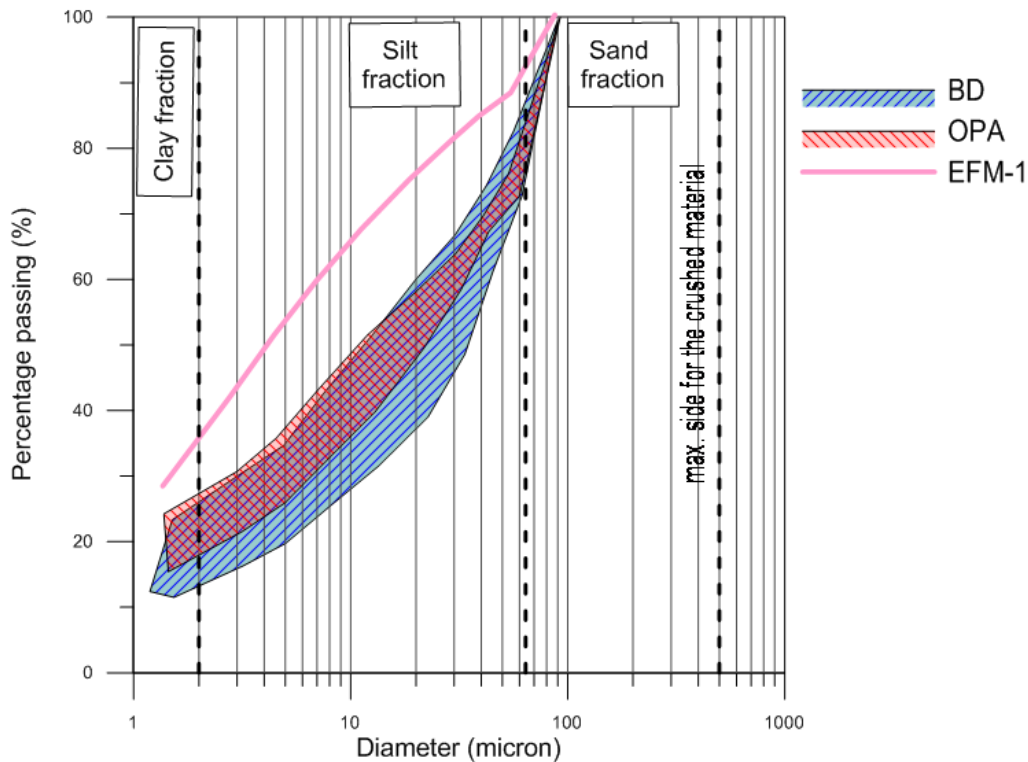


Fig. 3-5: Summary of the grain size distributions of the tested cores.

3.2 Pore size distribution – methods and results

Mercury Intrusion Porosimetry (MIP) was used to determine the Pore Size Distribution (PSD) for selected cores. The MIP technique consists in forcing the penetration of mercury inside a sample and measuring the intruded volume of mercury as a function of the applied pressure. The required pressure is inversely proportional to the size of the pores that are filled progressively. Washburn equation relates the applied pressure (P) to the equivalent diameter (D), assuming a circular shape for the pores) of the intruded porosity:

$$D = -\frac{4\sigma_{nw}\cos\theta_{nw}}{P} \quad (3-2)$$

where σ_{nw} and θ_{nw} are the surface tension and contact angle of the mercury.

Samples were cut from the cores by means of a saw. Typical dimensions for the samples are shown in Figure 3-6a. The MIP requires dry samples. To this regard, the samples were freeze-dried by sublimation inside a vacuum chamber (at 0 mbar and -50°C) for 24 hours, in order to minimize shrinkage effects upon drying (Figure 3-6b). For further information on freeze drying by sublimation, the reader is referred to the paper by Holzer et al. (2010). Once dried, the samples were placed inside the dilatometer which was directly inserted into the MIP apparatus (Figure 3-6c).

Tests were carried out using a Thermo Electron Corporations MIP apparatus. The apparatus uses two operating units: a low pressure (Pascal 140) and a high pressure (Pascal 440) unit.

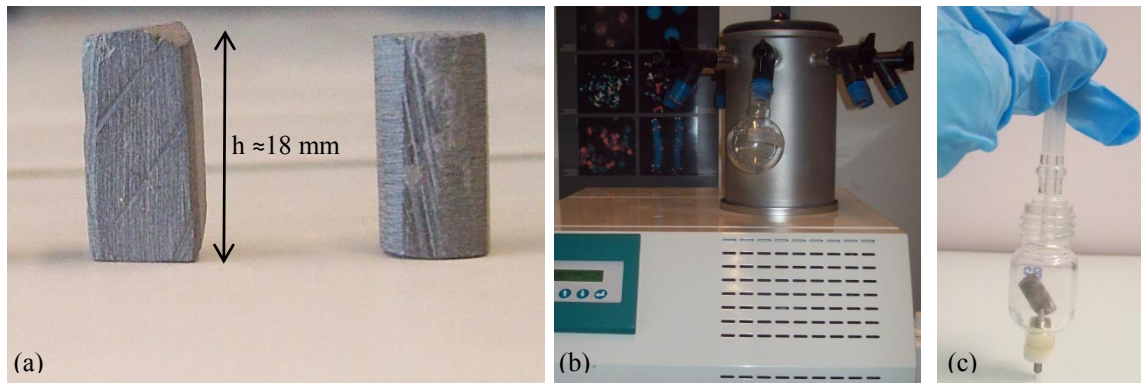


Fig. 3-6: Shale specimens for the MIP test (a), freeze-drying device (b) and dilatometer used for the analysis (c).

In the first part of the test, the Pascal 140 was used. Vacuum was first applied inside the dilatometer and the intrusion of mercury started at very low pressure. By the first filling of the dilatometer, the apparatus computed the volume of the sample. Incremental increasing pressure was then applied to the mercury (max. pressure is 100 kPa) and the intruded volume was recorded by the unit. At the end of measurements on the low-pressure unit, the dilatometer was transferred onto the high-pressure unit where the pressure was increased up to 400 MPa, corresponding to a pore radius of 1.8 nm. After the maximum pressure was reached, the pressure was progressively reduced and the extruded mercury volume was registered.

MIP tests were carried out for the cores BD-6, BD-16, BD-7, BD-30, OPA-3 and EFM-1.

Table 3-3 reports the properties of the tested samples before and after the freeze-drying. The obtained values for the BD-6 sample, in terms of initial density, water content and degree of saturation are in good agreement with the ones presented in Table 3-1. The samples EFM-1 and OPA-3 show a higher degree of disturbance.

Results from the MIP tests for all the considered cores are depicted in Figure 3-7 -Figure 3-12 in terms of cumulative intruded void ratio (ratio of the cumulative intruded mercury volume to the weight of the solid phase) and pore size density function versus the equivalent pore diameter (D). The (weighted) pore size density function (PSD) is the derivative of the cumulated intruded volume with respect to the logarithmic of the entrance pore diameter:

$$PSD = \frac{\Delta e_{HG}}{\Delta(\log d)} \quad (3-3)$$

where d is the entrance pore diameter and Δe_{HG} represents the void ratio intruded at each increment of the mercury pressure.

The cumulative void ratio graphs show that not the overall porosity is intruded and therefore investigated with the MIP test; this limit can be related to pores on the surface of the samples that are filled with mercury before the pressure increments start and to the smallest pores that require higher pressures to be intruded. The difference between the intrusion and extrusion volume could be associated to the entrapped ("constrained") porosity. It resulted in the range of 45 % - 52 % for all the BD samples, while it reached the value of 57 % in the OPA sample; for the EFM sample the entrapped porosity has a value of about 50 %. The PSD functions show that the modal pore size for the BD samples is in the range between 14 and 30 nm; the modal pore size for the OPA sample shows a value of 8 nm, about the same value is also observed for the

EFM core sample (Figure 3-13). The obtained results of the MIP analysis are reported in Table 3-4.

Tab. 3-3: Properties of the samples used for the MIP tests before and after the freeze-drying (F-D).

Core	before F-D				after F-D			
	ρ (Mg/m ³)	w (%)	E (-)	S_r (%)	ρ (Mg/m ³)	w (%)	E (-)	S_r (%)
EFM-1	2.53	1.0	0.06	44	2.50	~ 0	0.06	~ 0
BD-6	2.56	2.7	0.08	96	2.49	~ 0	0.08	~ 0
BD-16	2.42	1.2	0.12	29	2.39	~ 0	0.12	~ 0
BD-7	2.47	2.4	0.12	54	2.41	~ 0	0.12	~ 0
BD-30	2.54	1.0	0.10	28	2.51	~ 0	0.10	~ 0
OPA-3	2.49	2.6	0.13	57	2.42	~ 0	0.13	~ 0

Tab. 3-4: Summary of the results of MIP tests.

	Pore diameter at the Peak of PSD [μm]	Max cumulative intruded Void Ration	Constrained Porosity
EFM-1	8	0.05	50
BD-6	16	0.07	45
BD-16	18	0.04	44
BD-7	14	0.10	52
BD-30	30	0.07	49
OPA-3	8	0.09	57

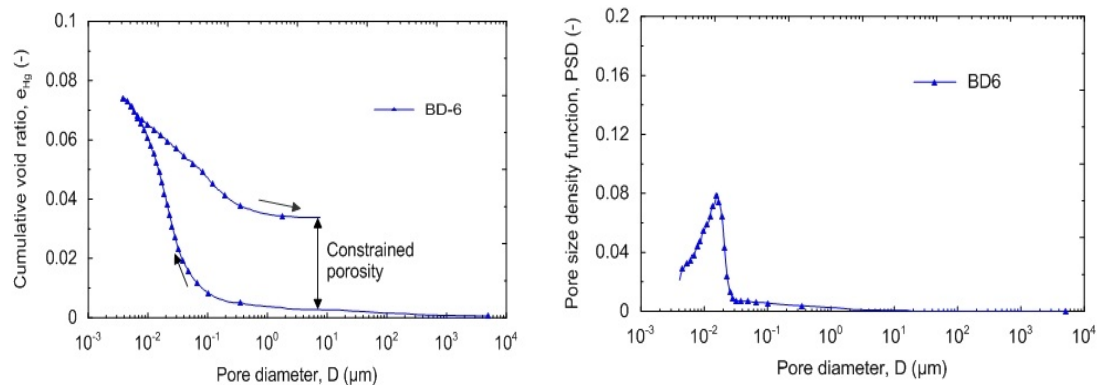


Fig. 3-7: Cumulative intruded void ratio and (weighed) pore size distribution for the sample BD-6.

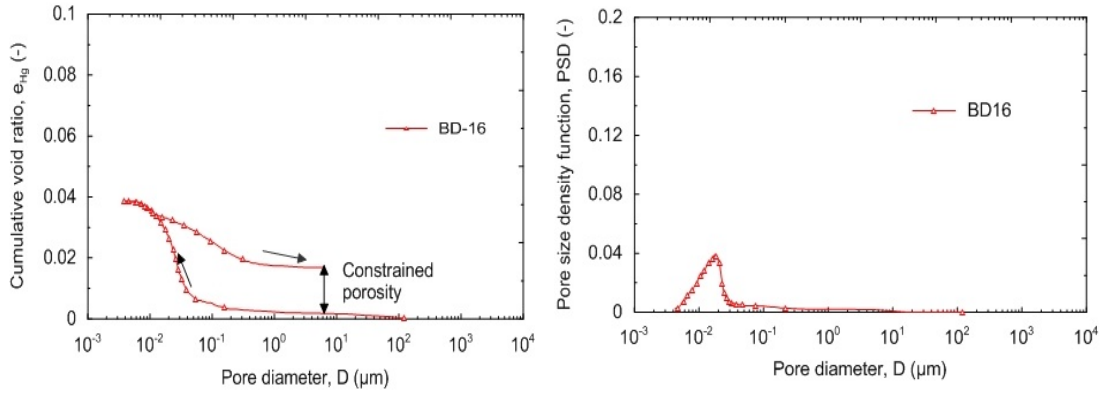


Fig. 3-8: Cumulative intruded void ratio and pore size distribution for the sample BD-16.

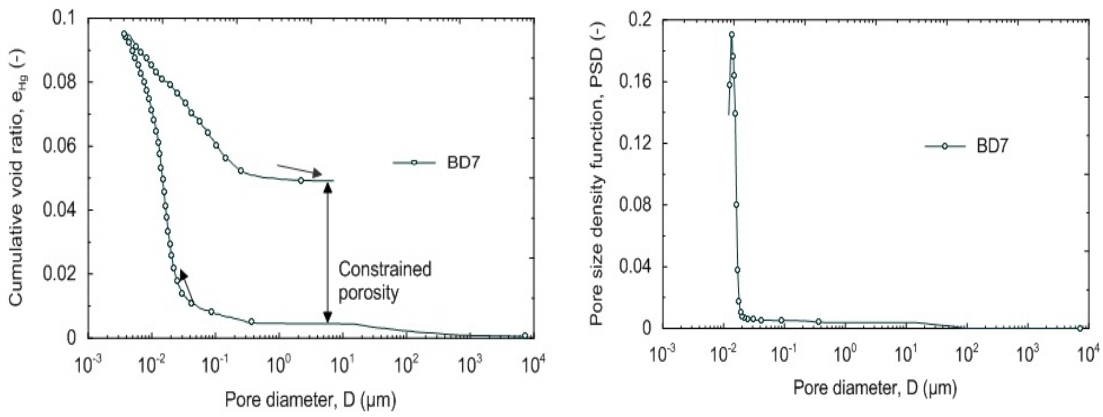


Fig. 3-9: Cumulative intruded void ratio and pore size distribution for the sample BD-7.

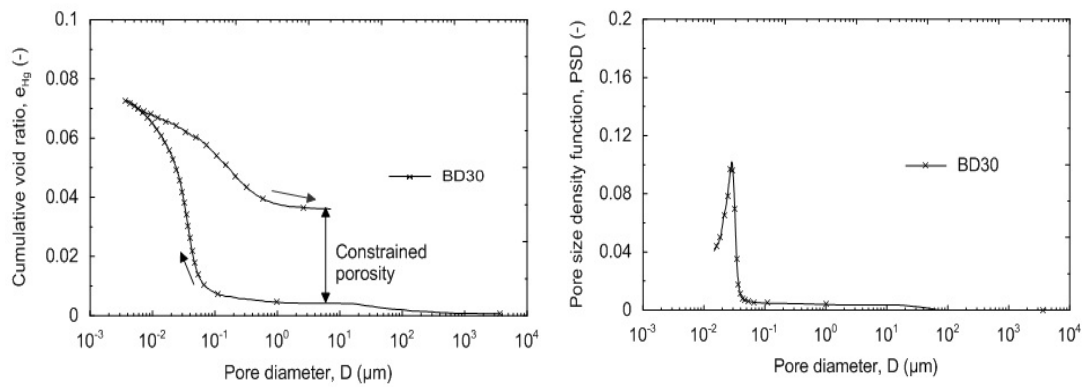


Fig. 3-10: Cumulative intruded void ratio and pore size distribution for the sample BD-30.

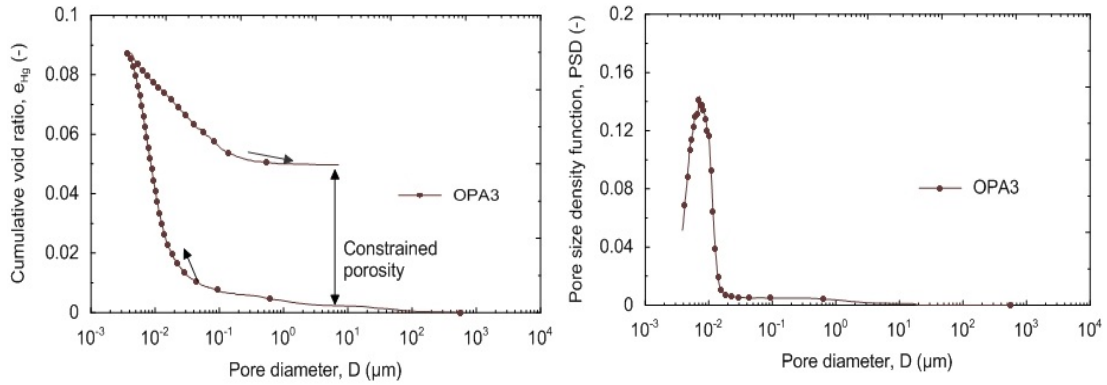


Fig. 3-11: Cumulative intruded void ratio and pore size distribution for the sample OPA-3.

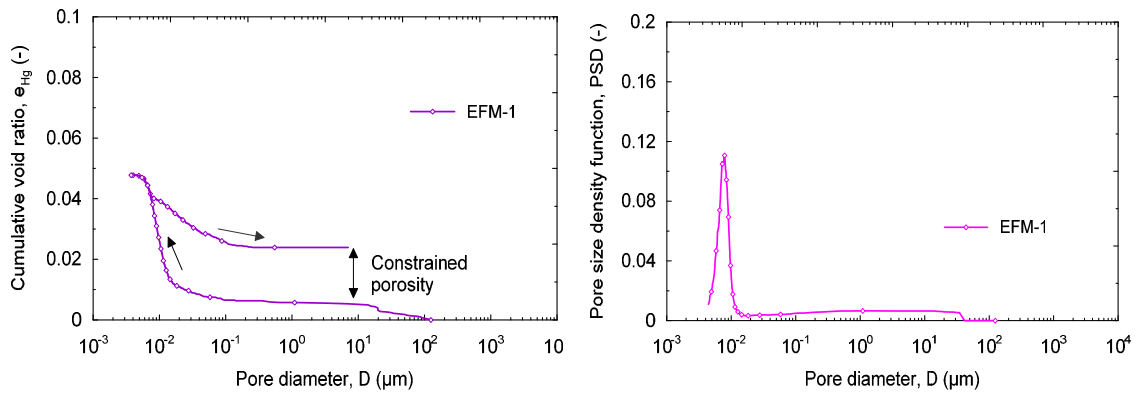


Fig. 3-12: Cumulative intruded void ratio and pore size distribution for the sample EFM-1.

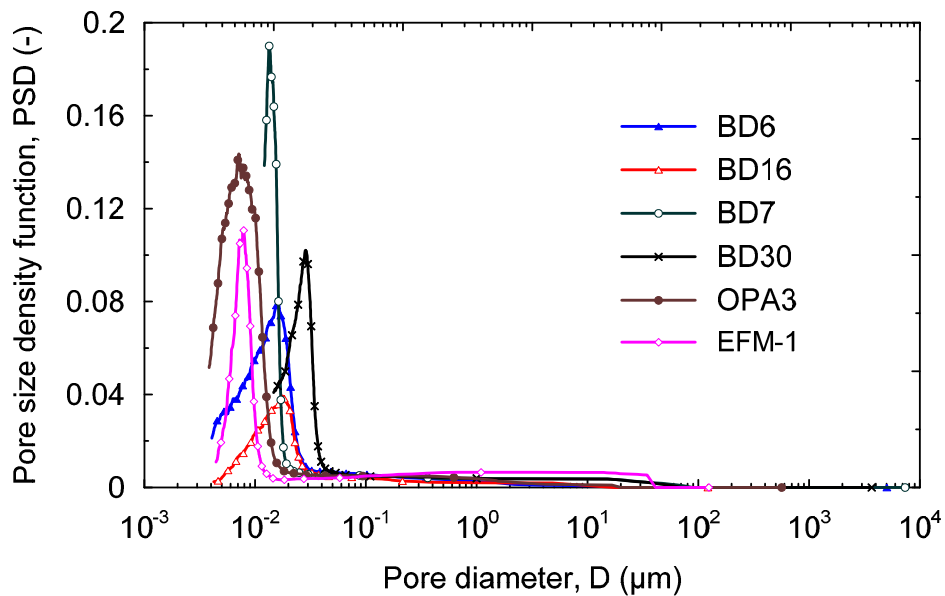


Fig. 3-13: Summary of the pore size distributions for all tested samples.

4 Water-retention behaviour

4.1 Methodologies

The retention curves for the cores were obtained by combining suction and volume measurements on samples prepared at different water contents in imposed main drying and wetting paths.

Suction reading was performed by means of a dew-point psychrometer (Decagon, WP4c) (Leong et al. 2003; Cardoso et al. 2007). The apparatus gives an indirect measurement of the total suction of a sample using the chilled-mirror dew-point technique and it is based on the relationship between the dew point and the relative humidity. A schematic representation of the device is shown in Figure 4-1. It consists of a sealed chamber where the following components are located:

1. a mirror, whose temperature is precisely controlled by a thermoelectric (Peltier) cooler;
2. a photoelectric cell, which detects the exact point at which the condensation first appears in the mirror;
3. an infrared thermometer, which detects the specimen temperature;
4. a fan, of which the purpose is to reach equilibrium more quickly and to control the boundary layer conductance of the dew point sensor.

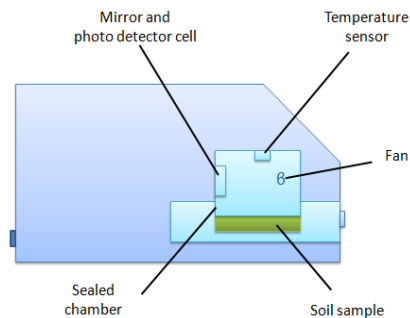


Fig. 4-1: Chilled-mirror dew point psychrometer.

The soil specimen, in equilibrium with the surrounding air, is placed in the sealed chamber. Consequently, the absolute humidity (mole fraction of vapour water) is defined. The temperature of the mirror is reduced without changing the absolute humidity by means of a thermoelectric cooler; the relative humidity rises accordingly. When the temperature in the mirror reaches the dew point, condensation occurs (which is observed by the photoelectric cell), at the same time, a thermocouple attached to the mirror records the dew point temperature. During the process, the air around the mirror is saturated gradually; while the mole fraction and the partial pressure of vapour water remain constant. Therefore, the saturated pressure of water vapour at the dew point temperature indicates the absolute humidity of the air. The relative humidity, which is the ratio between the saturated vapour pressure of water at the dew point and the saturated vapour pressure of water at air temperature, is obtained from the difference between the dew point temperature and the temperature of the sample. It is assumed that the two temperatures are measured simultaneously.

Initially the device was used to measure the initial total suction for all the cores. Obtained values are reported in Table 4-1. The high initial suction of the samples, together with the high degree of saturation can be seen as an indication for the excellent preservation of the cores prior to testing (absence of drilling induced microfracturing).

The following experimental procedures were established with the aim to have reliable protocols for the determination of the water retention curves for shales.

Tab. 4-1: Initial suction values.

<i>Core Name</i>	<i>Initial Suction ψ (MPa)</i>
BD-6	45.08
BD-16	37.45
BD-12	48.06
BD-18	45.44
BD-7	49.33
BD-30	134.71
OPA-3	73.62
OPA-2	66.26
OPA-20	51.35
OPA-6	69.45
OPA-18	68.93
EFM-1	100.89

4.1.1 Determination of the retention curves with investigation of the volumetric behaviour

For a proper determination of the retention curve shape for both paths (drying and wetting) it was decided to obtain 7 series of experimental points for 7 different target water contents; for each target value, 3 specimens at the same water content were tested using the WP4c to perform psychrometric readings (PR).

Before starting the measurement campaign, a test was carried out to quantify the water content loss rate for the investigated material exposed at the laboratory conditions ($t = 22^{\circ}\text{C}$, $\text{RH} = 50\%$ approx.) In this test, a slice with a typical thickness of 1 cm was dried for a few days while its weight was monitored. The curve obtained showed that the rate of loss of water is quite fast for high water content values so that only few minutes were necessary in order to lose about 0.5 % of water content; the rate of loss of water showed a significant decrease at low water content values and more than one day was necessary to lose the same amount of water content (0.5 %). The obtained results were used to set the time of exposition of the slices to the air, required to lose a given quantity of water from the samples.

In order to minimise disturbance to the sample, each slice was cut before unpacking; the external surface of each slice was then cleaned with a blade to remove the excess of paraffin penetrated into the core.

For each core, one slice (approx. 1 cm high) was used to determine the initial condition. Once the slice was cut, it was immediately divided in 5 parts (Figure 4-2). The central part (part III) was divided in three specimens which were immediately tested by means of the WP4c to evaluate the initial suction (Table 4-1). After the determination of suction, the volume of the three specimens was measured by means of the FDT (Fluid Displacement Technique) described in the followings. Finally, the initial water content, void ratio and degree of saturation, were calculated for each specimen. Part II and IV were used to obtain the suction values at maximum and minimum water content respectively (wet / dry state).

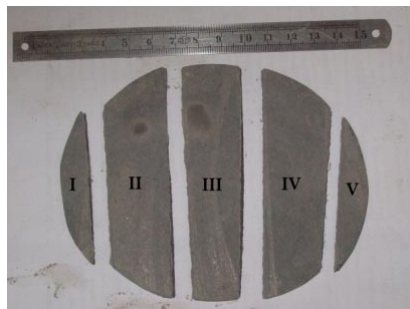


Fig. 4-2: Division of the slice in five parts.

Other slices were cut from the same core sample and placed in sealed-glass jars on a porous stone to obtain the main drying path. Porous stone and sample were separated by a filter paper (Figure 4-3). Synthetic water was used for equilibration. The water level covered completely the porous stone but without touching the soil slice so that the slice was wetted by capillary rise. During the wetting, the volume changes were allowed. Saturation using this procedure required nearly 2 weeks to obtain values close to 100 %.

Subsequently, the saturated slice was divided in 5 parts as shows in Figure 4-2, but only parts II, III and IV are kept in this phase. Each part was placed in a desiccator, and dried for a given amount of time until the desired water content was reached. During the drying procedure the water evaporated mainly from the external surface of the part; the samples were packed hermetically for approximately three days, to allow internal redistribution of water, before starting the suction measurements. Three specimens with approximately the same water content, were obtained from each part. The total suction of each specimen was measured using the WP4c and the specimen volume was measured using the FDT.

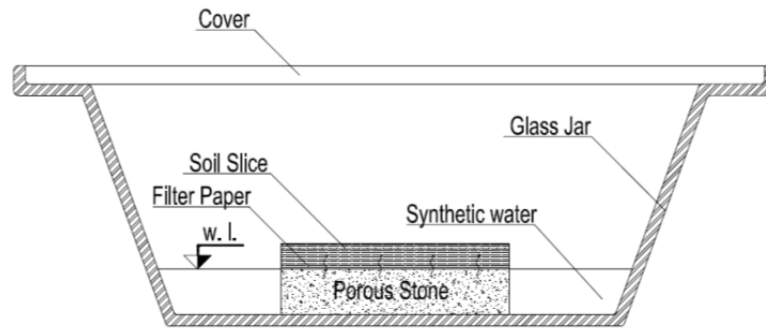


Fig. 4-3: Schematic representation of the system used to wet the samples.

A slice used to obtain the main wetting paths was initially placed in a desiccator and let to equilibrate to a very low value of RH imposed by means of silicate salts for approximately three weeks, until no further change in the weight of the slice was noticeable (Fig. 4-4a). Volume changes of the slice were allowed at this stage. Then the slice was cut in 5 parts. After dividing the parts, a given amount of synthetic water was added to each part at once in order to obtain the target water content. To have a better control on the mass of the added water, the water was dropped on the parts by using a syringe (Fig. 4-4b). Then each part was placed in a hermetic container for three days to allow internal redistribution of water. Finally, three specimens, at the same water content were obtained from each part and then tested (Fig. 4-4c).

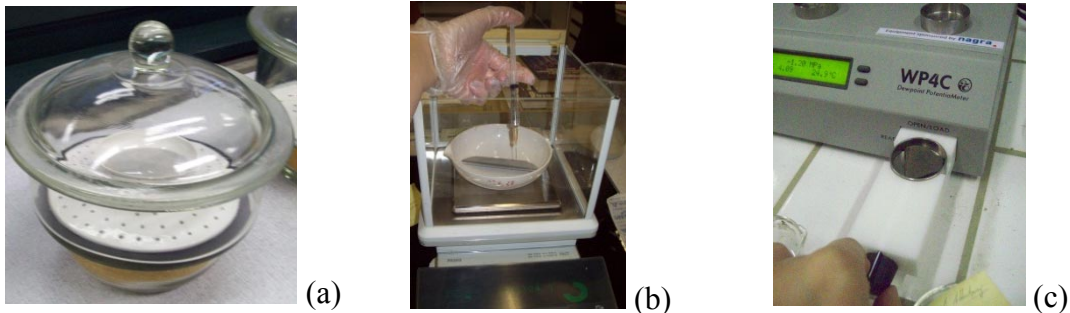


Fig. 4-4: Specimen preparation for the wetting path.

Volume measurements by the FDT

The method used to evaluate the volume of the specimens is based on the concept of fluid displacement (Figure 4-5). The fluid used was kerdane, which is a paraffin oil not miscible with water. A clean and dry pycnometer was filled with the oil and then weighed to know the mass of the kerdane-filled pycnometer (M_{pyc}) (Figure 4-5a). This operation was repeated at least 4 times, with the same filling technique, and an average value is considered.

The specimen, whose mass is known ($M_{spec,1}$), was put into the kerdane bath for the time required to let the fluid enter into the specimen voids, until no more bubble appeared in the bath (Figure 4-5b). The time required for this stage was approximately 4 hours. Then the specimen surface covered with-kerdane was wiped carefully with adsorbent paper to remove the excess of oil and the specimen was weighed again ($M_{spec,2}$) (Figure 4-5c). Finally, the specimen was placed into the empty pycnometer which was then filled using the same technique as before and weighed to obtain the mass of the pycnometer + wet-specimen + kerdane ($M_{pyc,2}$) (Figure 4-5d).

After these operations, the specimen was oven dried at 105 °C for 24 hours, to let the kerdane and the water, evaporate completely. The specimen was then weighed again to determine its dry mass (M_{dry}). The sample volume (V), the weight (G_s) and the volume of the solid phase (V_s) the water content (w), the void ratio (e), and the degree of saturation (S_r) were calculated with the following equations:

$$V = \frac{M_{pyc} + M_{spec,2} - M_{pyc,2}}{\rho_{ker}} \quad V_s = \frac{M_{dry}}{\rho_s} \quad w = \frac{M_{spec,1} - M_{dry}}{M_{dry}} \quad (4-1)$$

$$e = \frac{V - V_s}{V_s} \quad S_r = \frac{w \cdot G_s}{e} \quad (4-2)$$

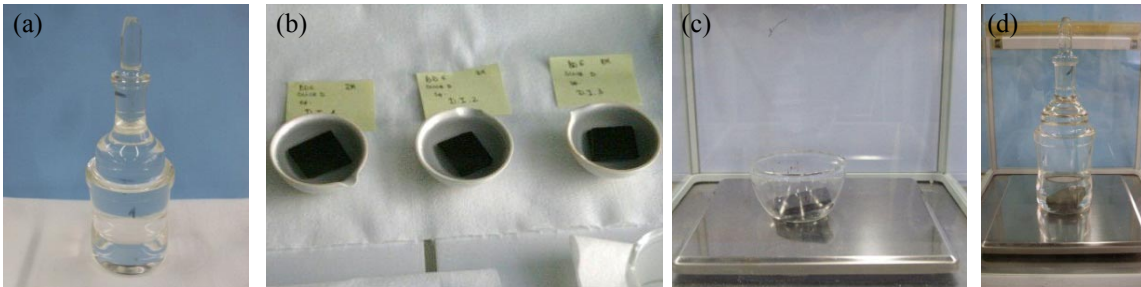


Fig. 4-5: Phases of the FDT for sample volume measurement.

4.1.2 Determination of the retention curves with progressive paths

The progressive procedure allow the determination of the wetting and drying paths of the retention curve using one single sample for each core: since the specimen could not be used for the volume measurement with the fluid displacement method (destructive technique), the retention curve was determined by progressive water content measurements in terms of psychrometric readings (PR) after each wetting/drying step. One of the main differences between the FTD method and the progressive water content measurements the fact that initial saturation or desiccation measurements are omitted, because the initial state of the material defines the starting point of the procedure. This procedure was preferred to the FTD technique in those cases when limited quantities of material was available for a given core.

Small samples measuring approximately 2 x 2 x 1 cm were cut and closed carefully in order to preserve the initial conditions. Three specimens for each of the tested cores were considered. The wetting paths were obtained first. Each sample was placed in a hermetic container and a certain amount of synthetic water was added to each sample to obtain the target water content. The containers were carefully closed in order to avoid any loss of water and a certain curing time (at least 48 hours) was allowed to ensure the internal equalization of the humidity. The psychrometric reading of total suction of each specimen was then performed using the WP4c dewpoint psychrometer. After the suction measurement, the next target for the addition of water was established.

The drying path started once the specimens reached a complete saturation, the samples were left to dry for a periode of time until a certain amount of water was lost; the samples were then closed hermetically to allow the internal redistribution of the humidity.

4.1.3 Summary of the applied procedures for the determination of the retention properties of the tested cores

The procedure applied for determining the retention properties for the various cores is listed in Table 4-2.

Tab. 4-2: Method for the determination of the retention curve and paths followed for each core (PR: psychrometric readings; FDT: Fluid displacement technique).

<i>Core Name</i>	<i>Hydraulic Path</i>	<i>Method</i>
EFM - 1	Wetting Drying	PR PR
BD - 6	Wetting Drying	PR + FDT PR + FDT
BD - 12	Wetting Drying	PR + FDT PR + FDT
BD - 18	Wetting Drying	PR + FDT PR
BD - 7	Wetting Drying	PR PR
BD - 30	Wetting	PR
OPA - 3	Wetting Drying	PR + FDT PR + FDT
OPA - 20	Wetting Drying	PR PR
OPA - 6	Wetting Drying	PR PR
OPA - 18	Wetting Drying	PR PR

4.2 Results

4.2.1 Water retention curves with investigation of the volumetric behaviour

The void ratio as a function of the total suction is presented in Figure 4-6 for the BD and in Figure 4-7 for the OPA. Despite the scattering, a tendency can be observed where the material shrinks when the suction increases and swells when suction decreases. In addition the evolution of the void ratios with the total suction shows that the porosity changes are more significant for the low range of suction variation. The evolution of the void ratio with suction reveals a slightly greater swelling of the OPA sample from the initial condition to the saturated state compared to the BD samples.

The results were fitted with the following incremental expression:

$$\dot{e} = -\frac{\psi}{K_{ref}} \left(\frac{\psi_{ref}}{\psi} \right)^m (1 + e_0) \quad (4-3)$$

where K_{ref} , Ψ_{ref} and m are the fitting parameters and e_0 is a reference void ratio. The previous expression is integrated so that the expression becomes as follows:

$$e = e_0 - \left[\frac{1}{(1-m)} \frac{\Psi_{ref}^m}{K_{ref}} (1 + e_0) \right] (\Psi^{1-m} - \Psi_0^{1-m}) \quad (4-4)$$

The obtained values of the parameters are reported in

Table 4-3 for both BD and OPA samples. The trends described by the previous incremental expression has been used to calculate the values of the degree of saturation S_r for all the BD core samples and OPA core samples using the corresponding set of fitting parameters of the two materials. The values obtained for each core were subsequently interpolated using the Van Genuchten's equation (1980):

$$S_r = \left(1 + \left(\frac{\psi}{P} \right)^\lambda \right)^{\left(\frac{1}{\lambda} - 1 \right)} \quad (4-5)$$

where P and λ are the fitting parameters. Curve fitting parameters for the shale samples where the water content evolution with suction has been determined during the performance of the fluid displacement technique (the 'Brown Dogger' samples BD-6, BD-12, BD-18 and the Opalinus Clay sample OPA-3) are reported in Table 4-4. Results in terms of water content and degree of saturation versus suction for the same samples are reported in Figure 4-8 - Figure 4-11.

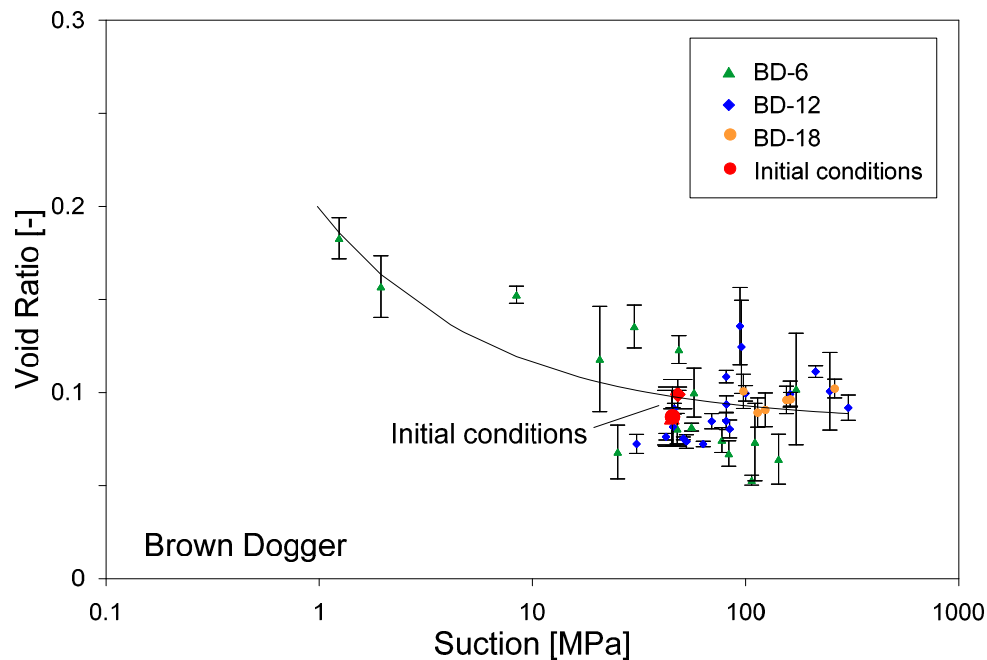


Fig. 4-6: Void ratio versus total suction for the cores from the 'Brown Dogger' formation.

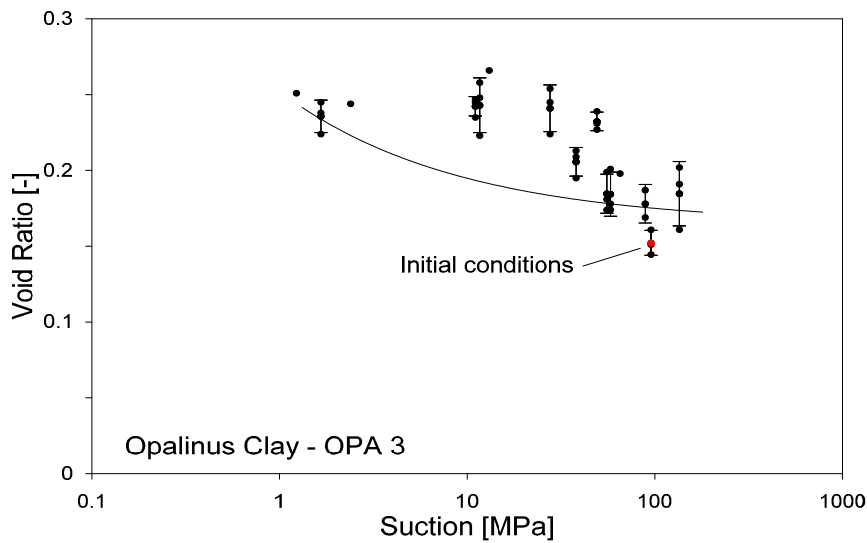


Fig. 4-7: Void ratio versus total suction for the cores from the Opalinus Clay formation.

The water content versus the total suction shows some hysterical behaviour; for a given suction value, an higher value of the water content is obtained for a drying path than in a wetting episode. Still the materials exhibit retention capacity for values of suction higher than 100 MPa. The initial state seems to rest on the drying path; this observation is accordance with the way in which the core was extracted and the samples were prepared. The curves for the BD and the OPA samples show an air entry value (gas entry pressure) at approximately 20 MPa (estimated on the main drying path for a degree of saturation equal to approx. 95 %).

Tab. 4-3: Fitting parameters for the evolution of the void ratio with the total suction.

	K_{ref} (MPa)	ψ_{ref} (MPa)	m (-)
BD	22.0	1.1	1.55
OPA	30	0.98	1.46

Tab. 4-4: Curve fitting parameters for the Van Genuchten equation for samples BD-6, BD-18, BD-12, OPA3.

Core	Parameter	Drying path	Wettin path
BD-6	P	57.2	35.9
	λ	2.8	2.4
BD-18	P	-	56.9
	λ	-	2.4
BD-12	P	-	63.86
	λ	-	2.46
OPA-3	P	13.87	38.19
	λ	1.53	1.77

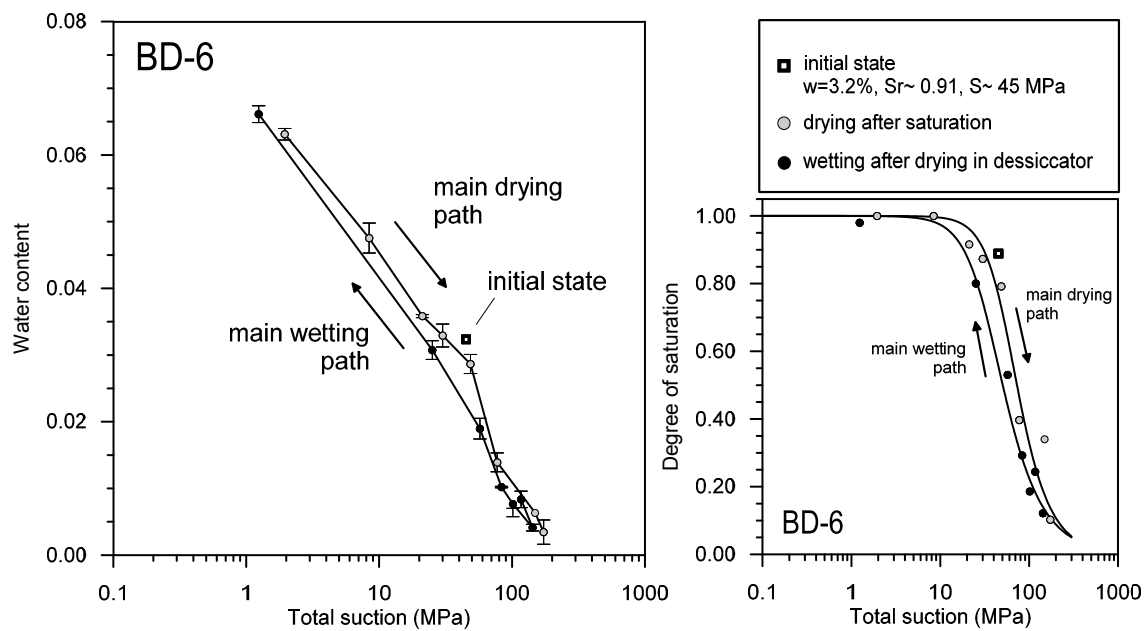


Fig. 4-8: Total suction versus water content and degree of saturation for the core BD-6.

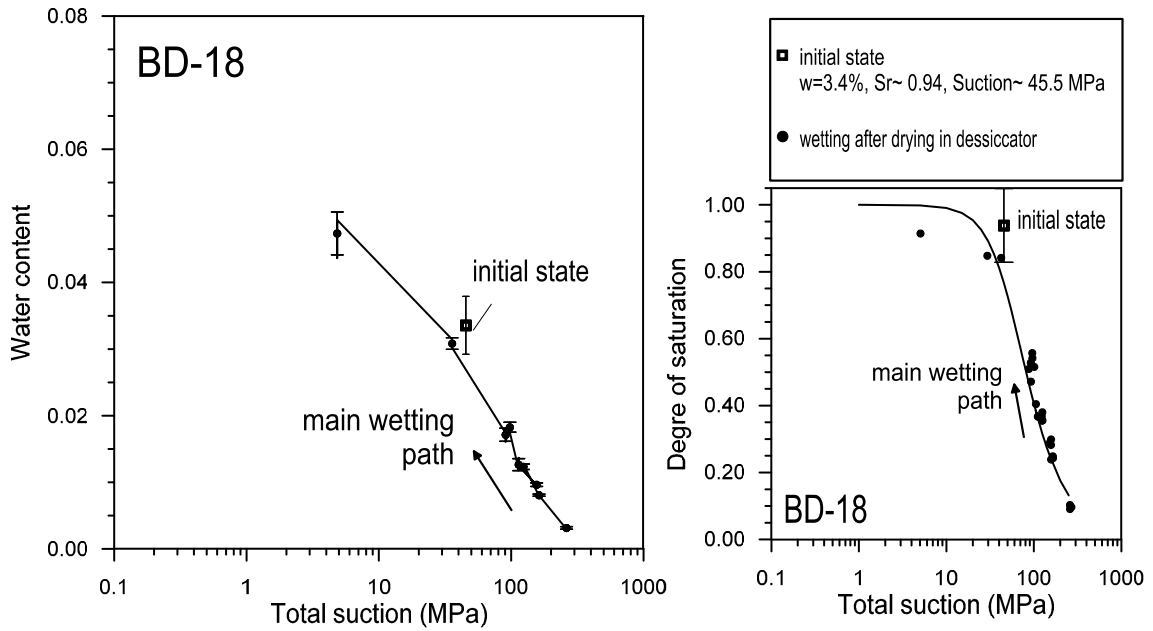


Fig. 4-9: Total suction versus water content and degree of saturation for the core BD-18.

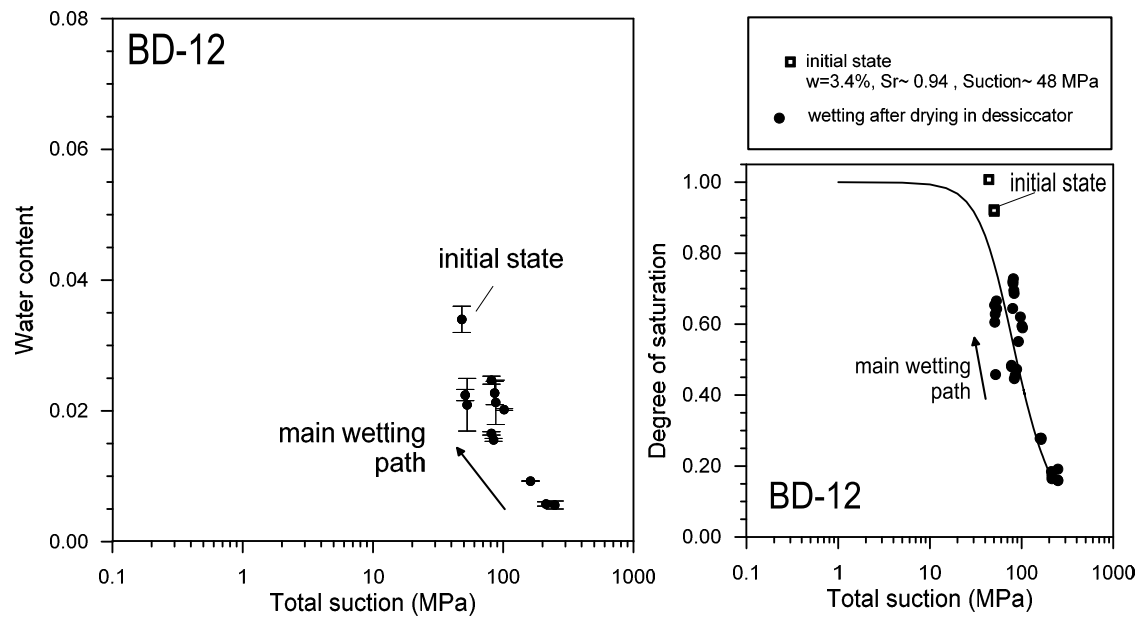


Fig. 4-10: Total suction versus water content and degree of saturation for the core BD-12.

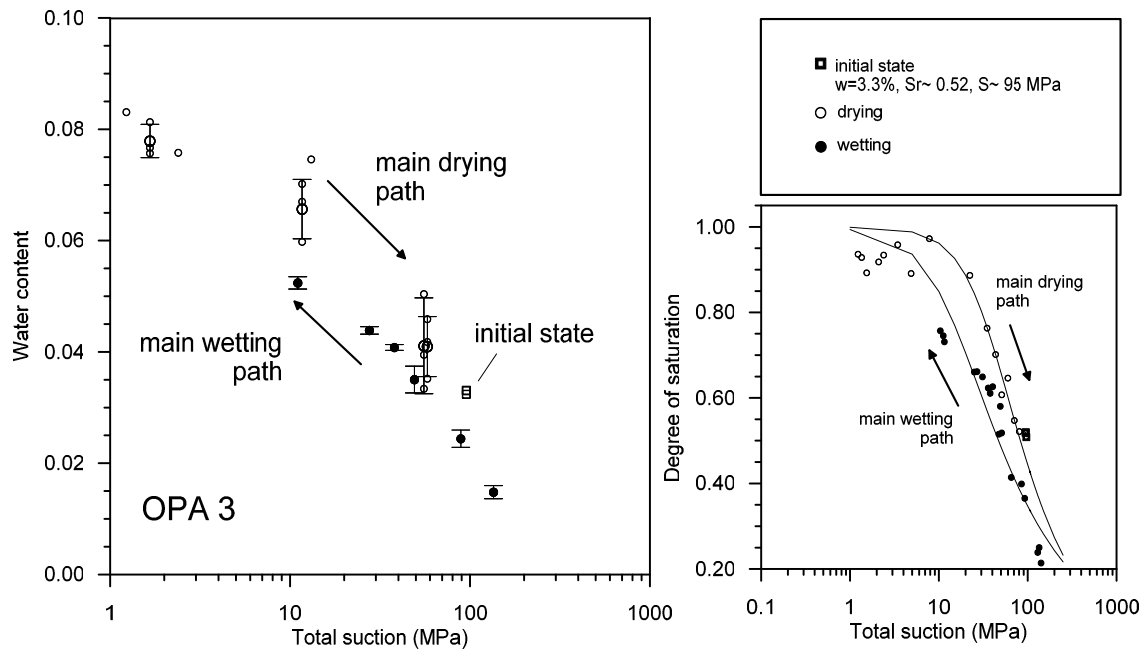


Fig. 4-11: Total suction versus water content and degree of saturation for the core OPA-3.

4.2.2 Water retention curves – progressive paths

The progressive path procedure is used to investigate the retention behaviour of the following cores: OPA-6, OPA-18, OPA-20, BD-7, BD-30, BD-18 (drying only) and EFM. As mentioned in Section 4.1.2 this technique allows to determine the complete main wetting and drying paths on a single specimen of each core and to clearly highlight possible hysteretical behaviours. Since the specimen could not be used for the volume measurement with the fluid displacement method (destructive technique), the retention curves were determined only in terms of water content by means of psychrometric readings (PR) after each wetting/drying step.

The evolution of the degree of saturation with total suction for the above mentioned samples has been determined considering the trend of the void ratio with suction of the two materials as defined in the previous section. The values of degree of saturation for both wetting and drying paths obtained for each core were subsequently interpolated using the Van Genuchten's equation. Curve fitting parameters for samples OPA-6, OPA-18, OPA-20, BD-7, BD-30, BD-18 (drying only) and EFM are reported in Table 4-4. Results in terms of water content and degree of saturation versus suction are reported in Figure 4-12 - Figure 4-14 for the BD core samples, while the results for the OPA samples are reported in Figure 4-15 - Figure 4-17.

Tab. 4-5: Curve fitting parameters for the Van Genuchten equation for samples BD-7, BD-30, BD-18, OPA-6, OPA-18, OPA-20.

Core	Parameter	Drying path	Wettin path
BD-7	P	69.19	27.87
	λ	2.09	1.69
BD-30	P	-	15.87
	λ	-	1.80
BD-18	P	76.19	-
	λ	1.79	-
OPA-6	P	57.19	19.27
	λ	1.71	1.47
OPA-18	P	60.19	25.87
	λ	1.77	1.49
OPA-20	P	57.19	18.87
	λ	1.81	1.46

The results show a well defined hysteretical behaviour since an higher value of water content and degree of saturation is obtained for the drying path compared to the wetting episode for a given suction value. The initial conditions of the samples are clearly localized on the main drying path; again this observation is in accordance with the way in which the core was extracted and the samples were prepared.

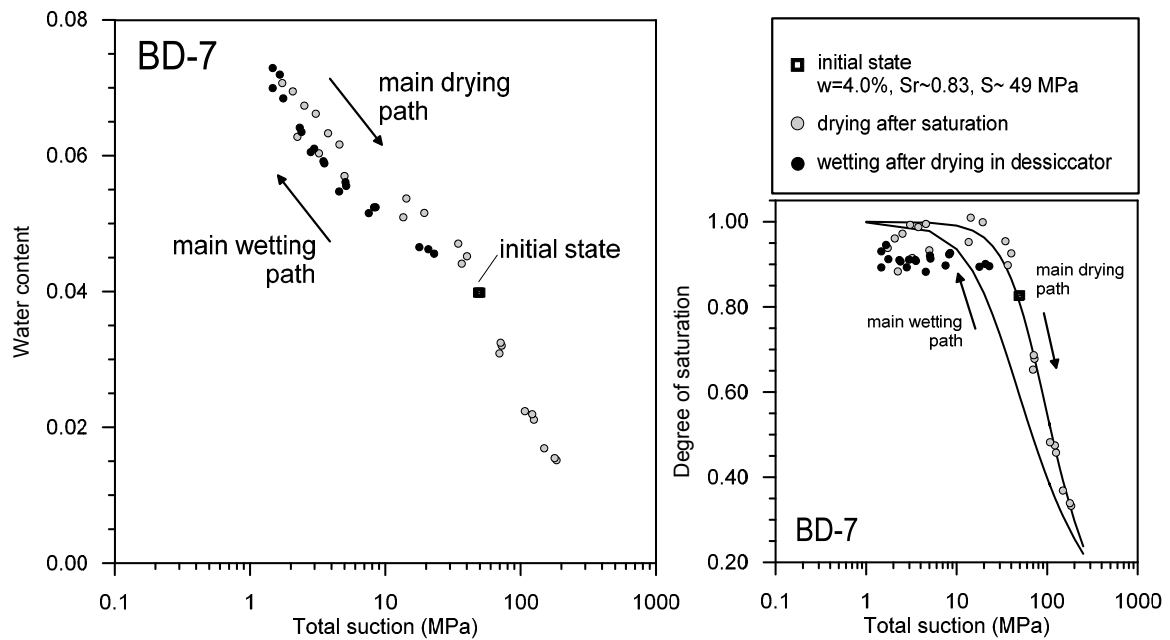


Fig. 4-12: Total suction versus water content and degree of saturation for the core BD-7.

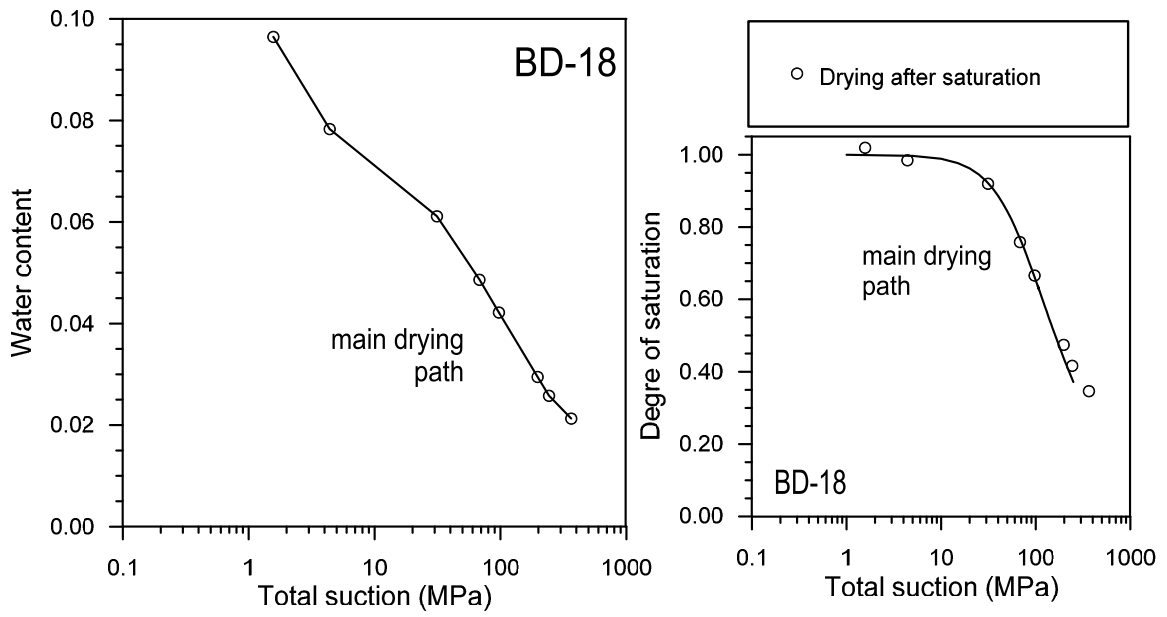


Fig. 4-13: Total suction versus water content and degree of saturation for the core BD-18 (drying path).

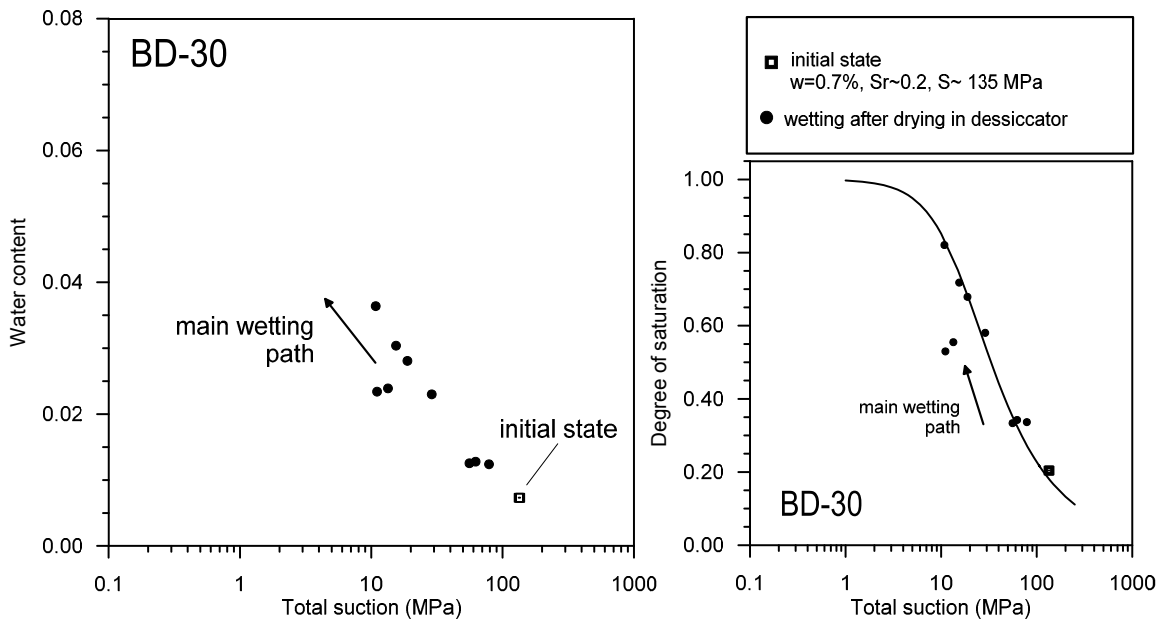


Fig. 4-14: Total suction versus water content and degree of saturation for the core BD-30 (wetting path).

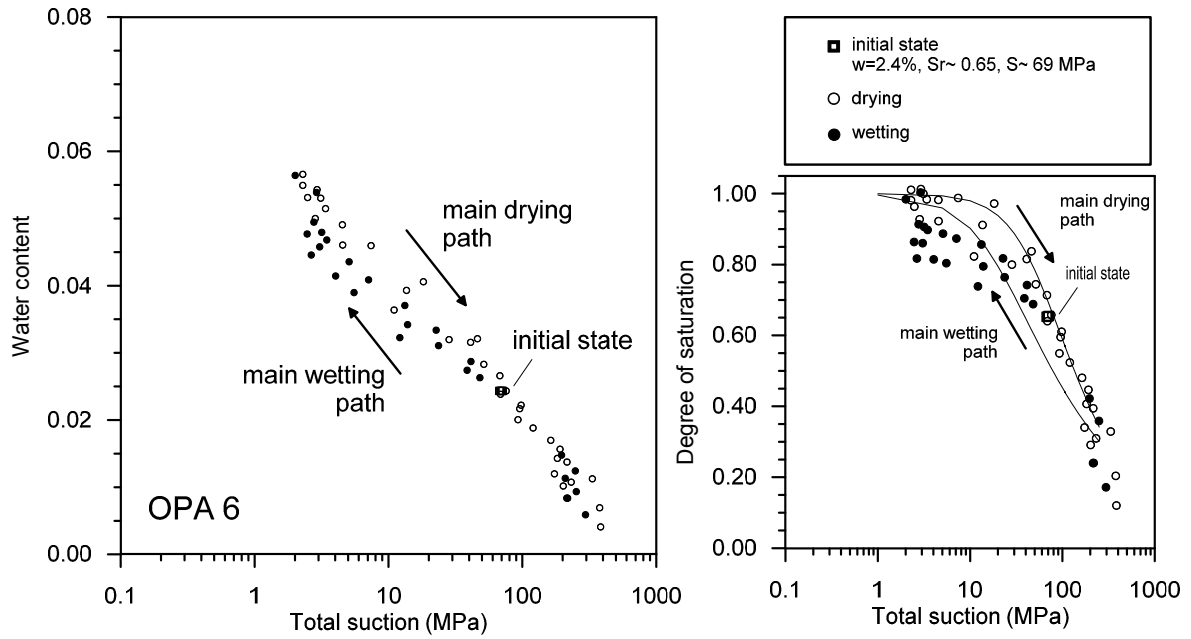


Fig. 4-15: Total suction versus water content and degree of saturation for the core OPA-6.

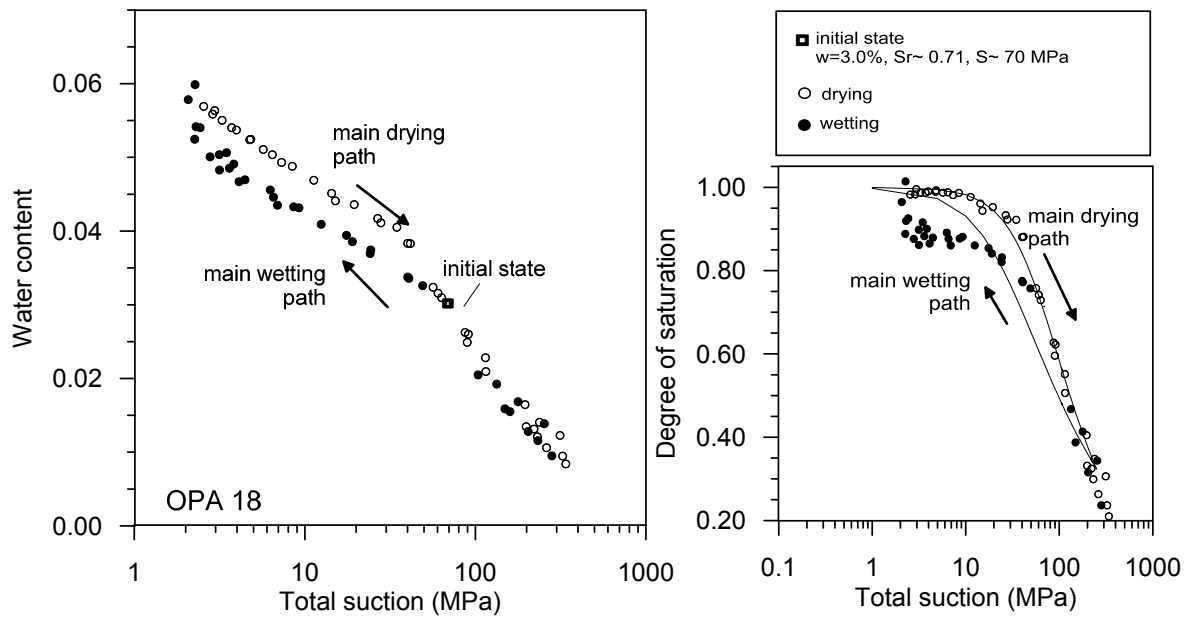


Fig. 4-16: Total suction versus water content and degree of saturation for the core OPA-18.

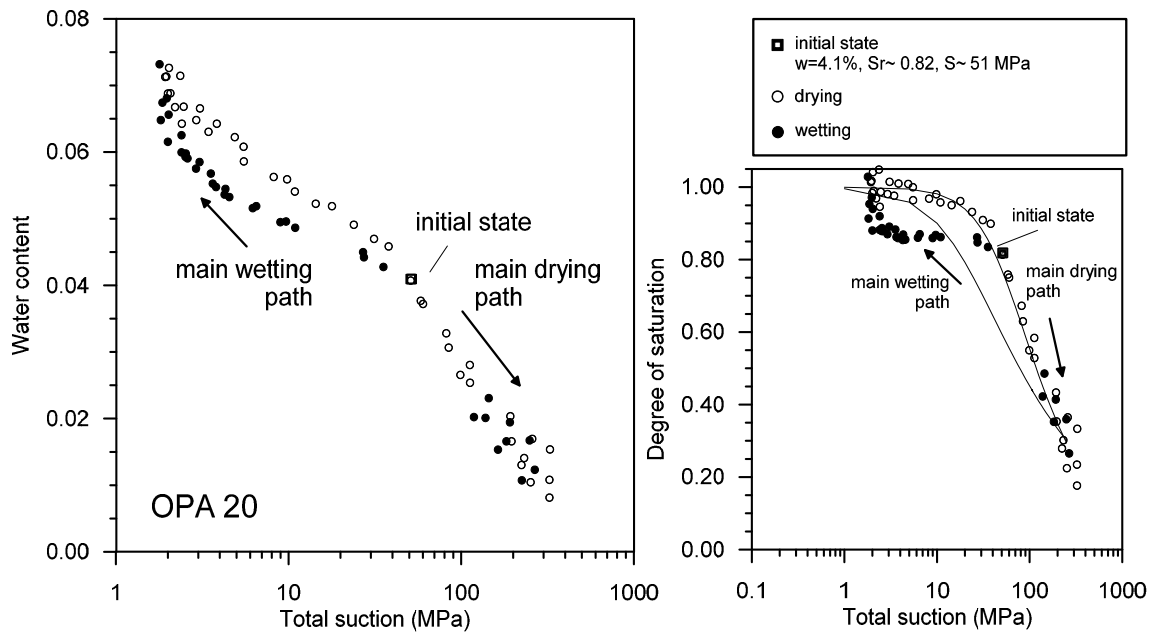


Fig. 4-17: Total suction versus water content and degree of saturation for the core OPA-20.

The retention curve in terms of water content versus total suction for the EFM-1 core sample is presented in Figure 4-18.

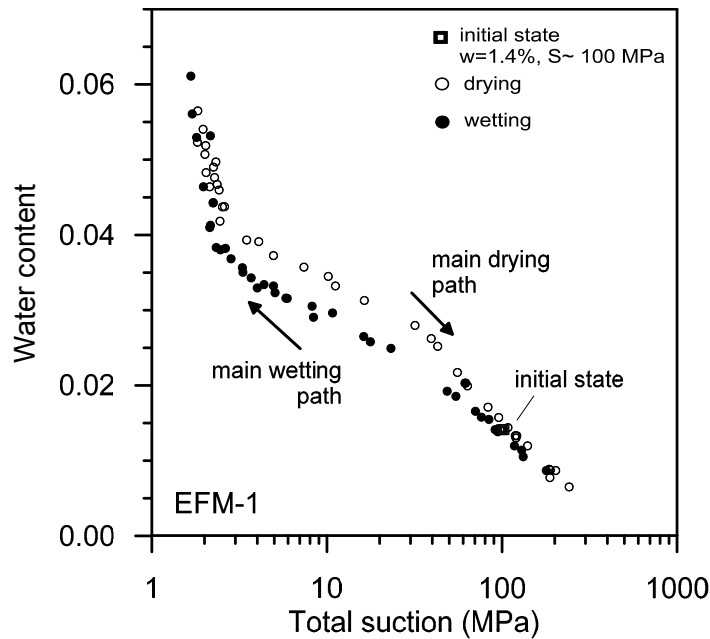


Fig. 4-18: Total Suction versus water content for the core EFM-1.

As for the BD and OPA samples, the results for EFM-1 core sample show a well defined hysterical behaviour and the initial conditions of the sample are clearly localized on the main drying path.

5 Hydro-mechanical tests

Performed hydro-mechanical tests included:

- Assessment of the swelling behaviour;
- Volumetric response upon 1D loading at high vertical stress.

5.1 Sample preparation procedure

The following procedure was developed and systematically applied to obtain the specimens for the swelling and the oedometric tests (Figure 5-1). A slice with a thickness of approximately 20 mm was sawn without unpacking the core to minimize the disturbance to the sample as shown in Figure 5-1.a. Since the materials exhibited a tendency to crack during re-coring, the diameter of the slice was progressively reduced in order to obtain a disk with a diameter slightly larger than the final confining ring (Figure 5-1.b). Final re-coring was performed by using a hydraulic press (Figure 5-1.c). Finally, the lower and upper faces were smoothed using sand paper (Figure 5-1.d) in order to obtain parallel and plane surfaces (Figure 5-1.e).



Fig. 5-1: Specimen preparation for swelling and oedometer tests.

5.2 Swelling tests

The swelling behaviour (perpendicular to bedding) was analysed by means of free and constrained swelling tests. High-rigidity steel cells, with an internal diameter of 78.50 mm, were employed to ensure oedometric conditions. Inside the cell, the specimen rested on a porous plate and filter paper, through which the pore water pressure on the specimen lower base could be controlled.

The layout for the free swelling test was completed by means of a filter paper and a rigid porous plate resting on the upper base of the specimen, on which a LVDT (Linear Variable Differential Transformer with a resolution of 1 μm and a working range of 40 mm) was placed to continuously record the swelling heave by an automatic acquisition system. The superior part of the cell was completely covered by a plastic film in order to limit evaporation from the specimen. Synthetic water was added on both bases of the specimen. The water is injected using a pressure-volume (PV) controller connected to the base of the cell. The base of the cell is connected to a flushing line, allowing the elimination of air bubble eventually entrapped in the base of the cell.

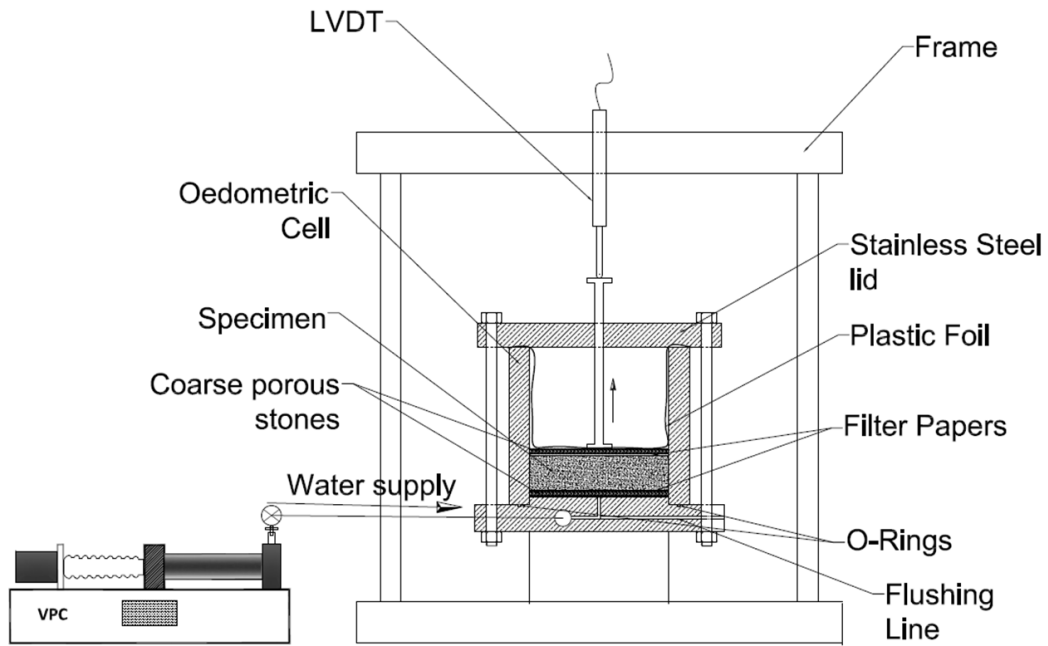


Fig. 5-2: Experimental setup for free swelling tests.

When constrained tests were performed, the cell was placed in a high rigidity frame providing isochoric conditions during the wetting. Three screws are used to compress the O-ring placed between the ring and the bottom plate, hence any leakage is prevented.

In this case, the upper base was in contact with a load ram connected to the frame. An initial vertical stress of few kPa was applied to ensure a good contact between the specimen and the load ram. A load cell, placed above the apparatus, allowed the continuous measurement of the vertical force developing during the wetting and the computation of the swelling pressure (with a resolution of 1 kPa referred to the specimen area). A PVC lid on the top of the cell prevents the evaporation of the water from the upper base of the specimen during the test. A micrometer was placed above the frame to detect unwanted volume changes during the swelling.

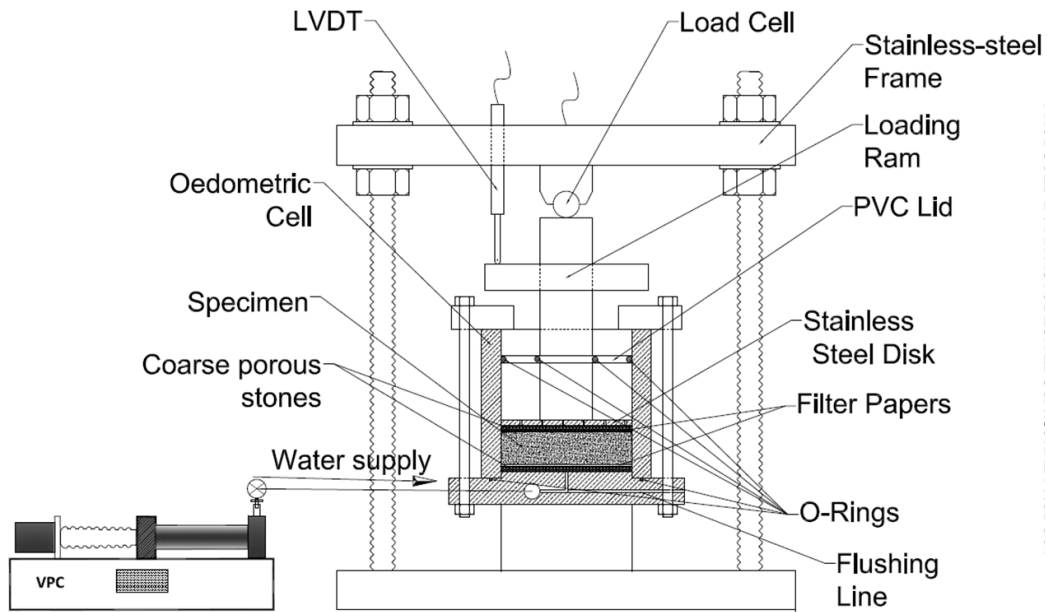


Fig. 5-3: Experimental setup for constrained swelling tests.

The list of the performed tests and the initial properties of the samples is reported in Table 5-1.

The constrained swelling tests were carried on considering the correction of the vertical deformations of the apparatus. The correction procedure consists in the compensation of the axial displacements of the apparatus (which are measured by the LVDTs) when the axial strain exceeds the value of about 0.1 %. The correction procedure is showed for the test on the OPA-6 core in Figure 5-4, where the evolutions of the swelling pressure and of the axial strain are reported. A maximum swelling pressure of 944 kPa was recorded.

Results for the constrained swelling tests on samples BD-16, BD-18, OPA-2 and OPA-18 are depicted in Figure 5-5 - Figure 5-9. The final values of the swelling pressure for each core are reported in Table 5-2.

Results of the free swelling tests on a BD sample (BD-18) and on an OPA sample (OPA-20) are reported in Figure 5-10 and Figure 5-11; they show a free swelling of 7.9 % for the BD material and of 10.75 % for the Opalinus Clay material. These results are in good agreement with the swelling/shrinkage behaviour described by the void ratio distribution in respect to suction which is observed in the water retention analysis (Section 4.2.1).

Tab. 5-1: Performed swelling tests and initial properties of the samples.

Core	Test condition	ρ (Mg/m ³)	w (%)	e (-)	S_r (%)
BD-16	Constrained swelling	2.55	1.1	0.09	35
BD-18	Free swelling	2.51	2.5	0.12	58
BD-18	Constrained swelling	2.51	2.5	0.12	57
OPA-2	Constrained swelling	2.49	4.9	0.16	87
OPA-6	Constrained swelling	2.53	2.9	0.11	70
OPA-18	Constrained swelling	2.52	2.9	0.12	68
OPA-20	Free swelling	2.44	2.5	0.15	45
OPA-20	Constrained swelling	2.50	3.1	0.13	65

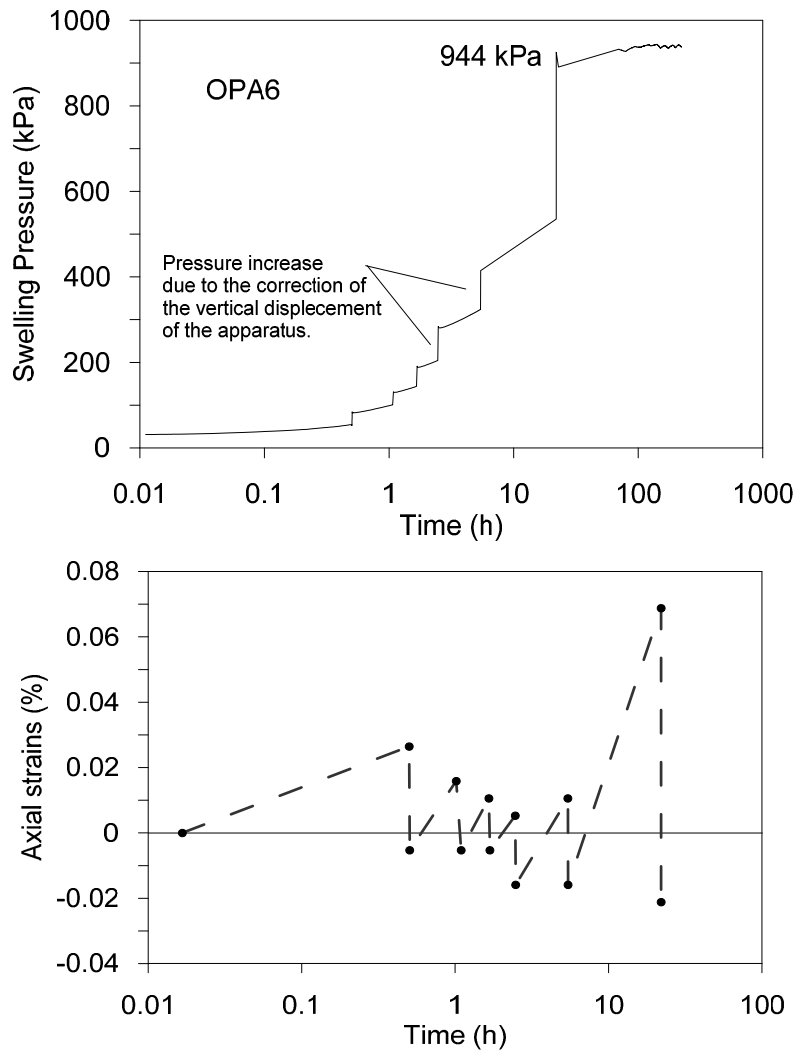


Fig. 5-4: Evolution of the swelling pressure and axial strain in the constrained swelling test on sample OPA-6.

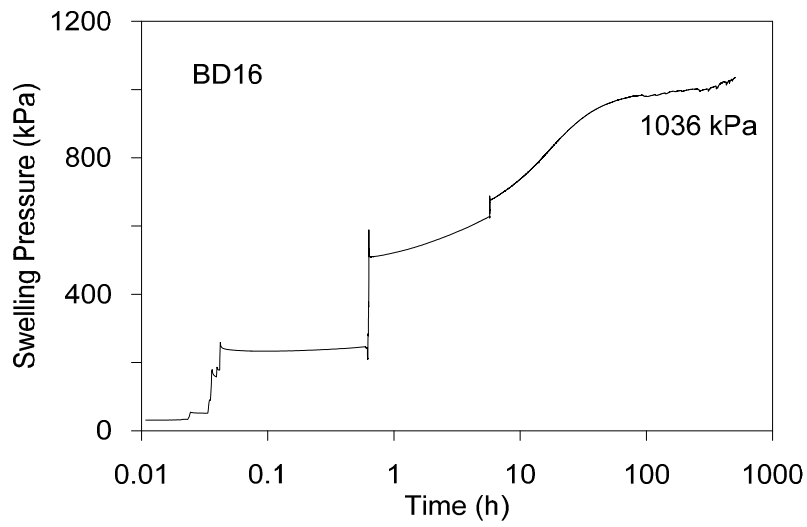


Fig. 5-5: Constrained swelling tests on sample BD-16.

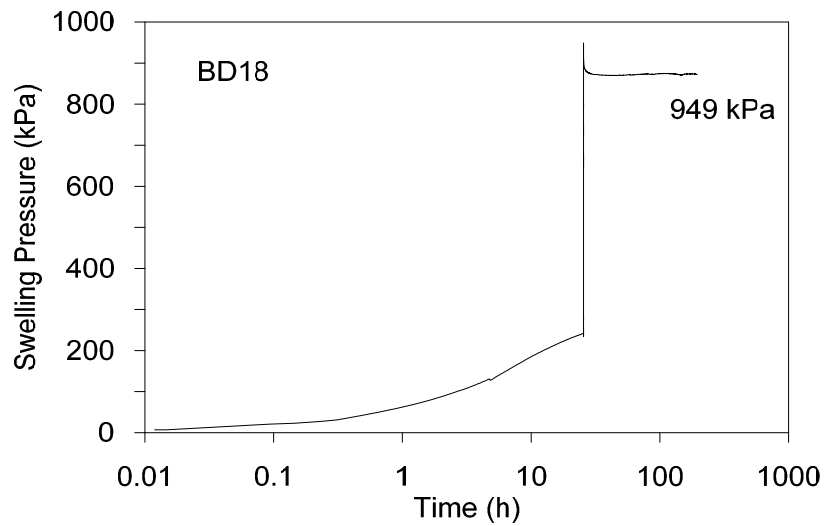


Fig. 5-6: Constrained swelling tests on sample BD-18.

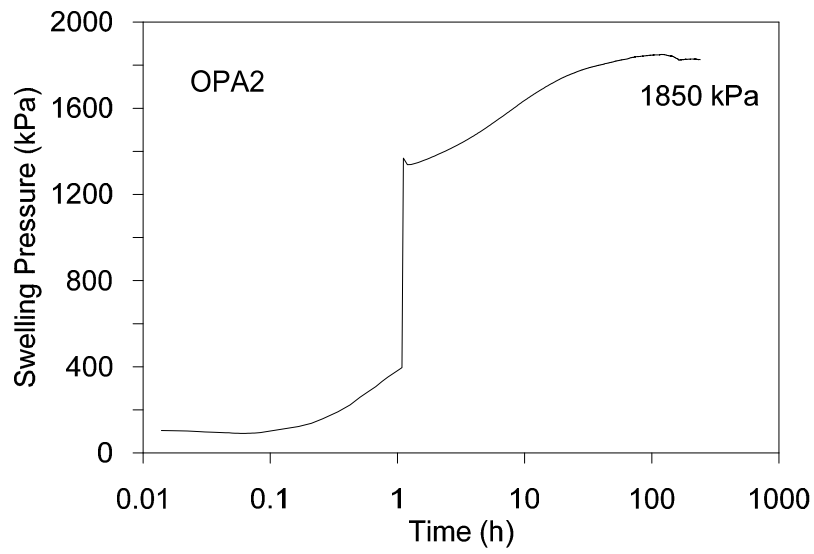


Fig. 5-7: Constrained swelling tests on sample OPA-2.

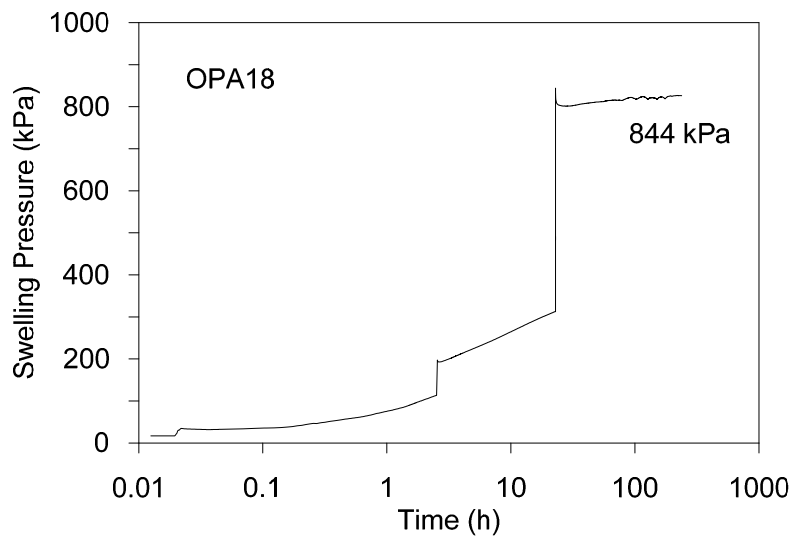


Fig. 5-8: Constrained swelling tests on sample OPA-18.

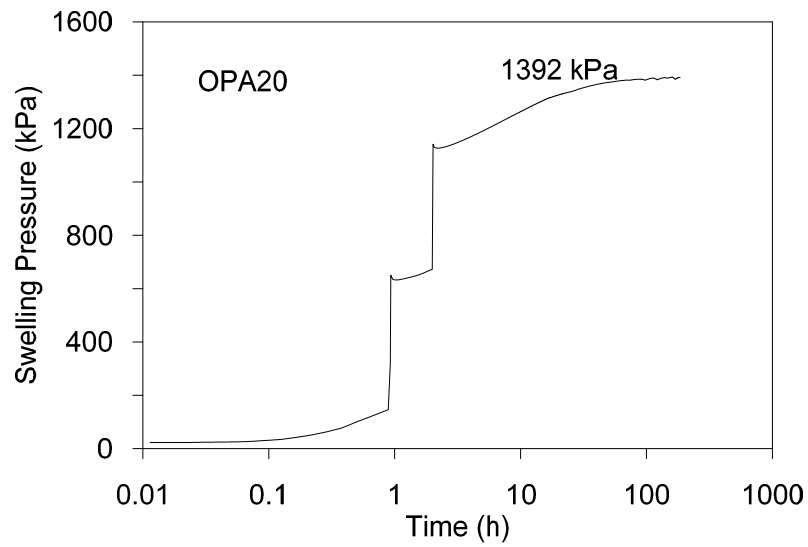


Fig. 5-9: Constrained swelling test on sample OPA-20.

Tab. 5-2: Swelling Pressure of the tested samples.

Core	Swelling pressure (kPa) (Constrained swelling tests)
BD-16	1036
BD-18	949
OPA2	1850
OPA6	944
OPA18	844
OPA20	1392

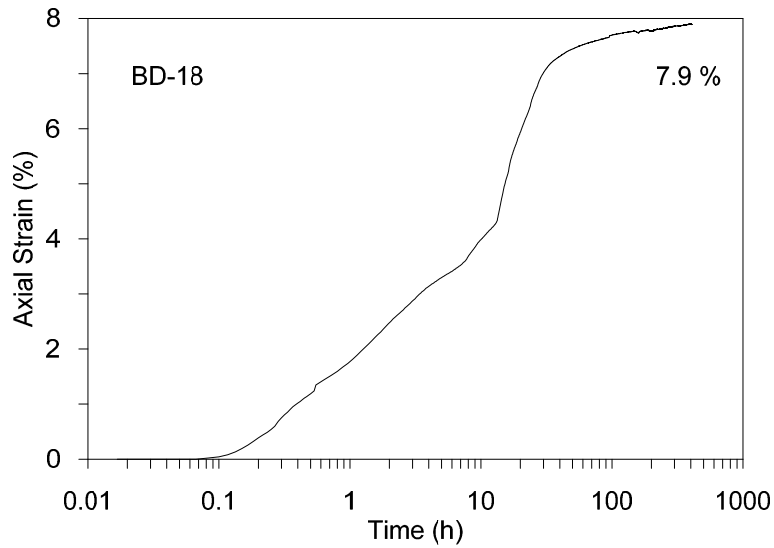


Fig. 5-10: Free swelling test on sample BD-18.

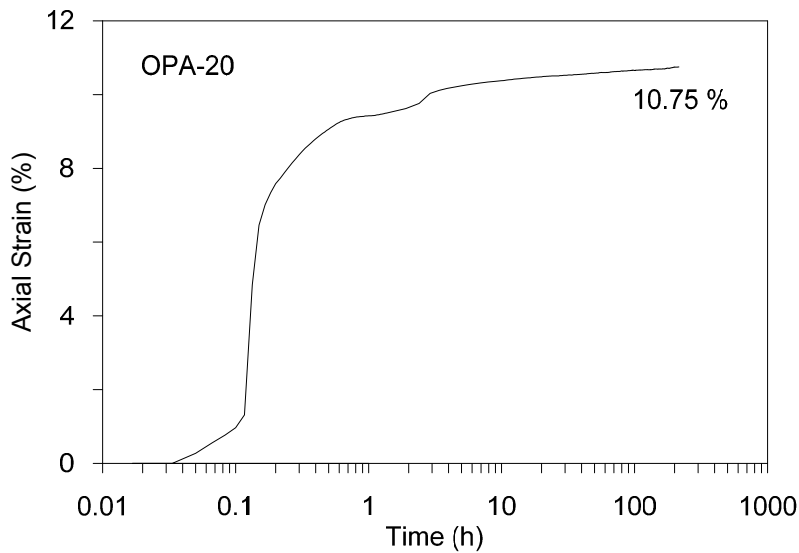


Fig. 5-11: Free swelling test on sample OPA-20.

5.3 High-pressure oedometric tests

High-pressure oedometer tests were carried out on the cores BD-6, BD-16, BD-12, BD-7, OPA-2, OPA-20, OPA-6 and OPA-18. The apparatus used for these tests is a specially designed high-pressure oedometer cell allowing a maximum attainable vertical stress of 100 MPa (Salager et al. 2010; Ferrari and Laloui, 2012). The high level of applicable vertical stress was required in order to observe the transition from the pre- to the post-yield behaviour of the material.

The layout and a picture of the apparatus are depicted in Figure 5-12. The vertical pressure is applied by means of a hydraulic jack, in which the pressure is maintained by a pressure/volume controller.

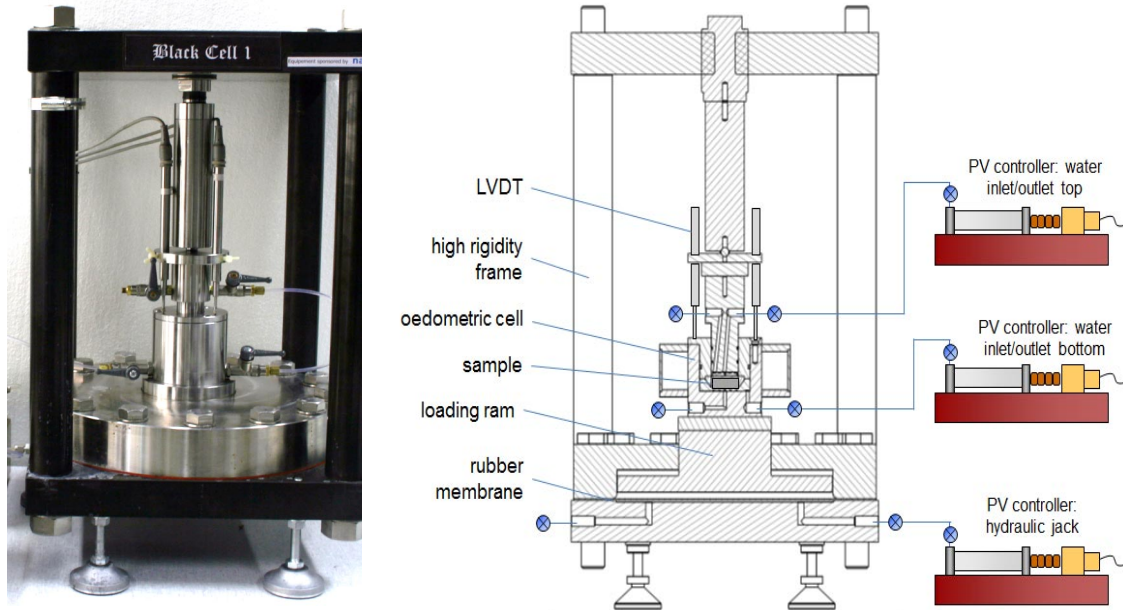


Fig. 5-12: The high pressure oedometric cell at the LMS-EPFL.

The ratio between the surface of the hydraulic jack and the one of the specimen was designed in order to amplify the pressure provided by the controller up to 100 MPa (the accuracy in the vertical stress control is about 0.06 MPa). The vertical displacement is measured via three LVDTs fixed on the loading piston and in contact with the base of the cell (accuracy of 1 μm). The tests were performed in drained conditions.

During the test, a delay in the application of the vertical load was observed due to the time requested by the controller in applying the target pressure. In order to cope with this delay, an analytical method to process the consolidation induced by a non-instantaneous application of the load was developed and applied to interpret the settlement versus time curves.

Table 5-3 reports the list of tested samples along with their initial properties. Samples were initially equilibrated at constant volume applying a 50 kPa water pressure at the two bases. Measured swelling pressure values are reported in Table 5-4 while a comparison between the values of swelling pressure developed in the oedometric cell and those obtained during the constrained swelling tests is shown in Figure 5-13.

Afterwards two loading-unloading cycles are performed in steps, allowing complete dissipation of the excess pore water pressure (drained conditions).

The oedometric curves for the BD cores, along with the determination of the vertical yield stress and the swelling and compression coefficients are reported in Figure 5-14 - Figure 5-17 in terms of axial (or vertical) strain versus applied vertical effective stress. All the curves show similar results in terms of compression and swelling coefficients and exhibit a vertical yield stress in the range of 16-20 MPa. A systematic increase of the swelling coefficient with the preconsolidation pressure is observed.

The oedometric curves for the OPA cores, along with the determination of the vertical yield stress and the swelling and compression coefficients are reported in Figure 5-18 - Figure 5-21 in

terms of axial (or vertical) strain versus applied vertical effective stress. In this case almost all the curves show similar results in terms of compression and swelling coefficients, slightly different results are observed in the OPA-6 core where the compression and swelling coefficients show lower values (Figure 5-22 and Figure 5-23); this is probably due to the presence of fine sandy layers at the depth at which the OPA-6 core is extracted (882.20-882.50 m) (Table 2-1).

All the curves for the Opalinus Clay formation exhibit a vertical yield stress in the range of 19-24 MPa. Again a systematic increase of the swelling coefficient with the preconsolidation pressure is observed.

Tab. 5-3: Initial characteristics of the specimens tested in the high-pressure oedometric cell.

Core name	Initial ρ [g/cm ³]	Initial w [%]	Initial e [-]	Sr (%)
BD- 6	2.58	3.0	0.07	100
BD-7	2.51	3.3	0.11	79
BD-16	2.46	3.4	0.12	75
BD-12	2.55	3.5	0.11	90
OPA2	2.45	4.2	0.15	75
OPA6	2.51	2.5	0.11	62.9
OPA18	2.51	3.2	0.11	77.9
OPA20	2.49	3.5	0.13	73

Tab. 5-4: Measured values of the swelling pressure in the high pressure oedometer tests. Swelling pressures were determined in the initial phase of sample saturation by applying of a low water pressure of about 50 kPa.

Core	Swelling pressure (kPa)
BD-6	370
BD-16	570
BD-12	260
BD-7	1107
OPA2	1371
OPA20	685
OPA6	911
OPA18	651

The systematic increase of the swelling coefficient with the preconsolidation pressure can be observed in Figure 5-22 where the swelling coefficients are plotted against the maximum attained vertical effective stress for the 'Brown Dogger' and for the Opalinus Clay cores. The values of the coefficient of compressibility for all the tested cores along with the corresponding vertical effective stress are plotted in Figure 5-23. The lower compressibility of the OPA-6 core compared to the other cores from the Opalinus Clay formation can be observed. The previous considerations are summarized in Table 5-5 where the yield stress, coefficients of compressibility and swelling coefficients are listed for all the tested cores.

The results of the high pressure oedometer tests in terms of oedometric modulus and coefficient of consolidation versus vertical effective stress for each tested core are presented in Figure 5-24 - Figure 5-31. All the results are plotted in Figure 5-32 for the 'Brown Dogger' and in Figure 5-33 for the Opalinus Clay.

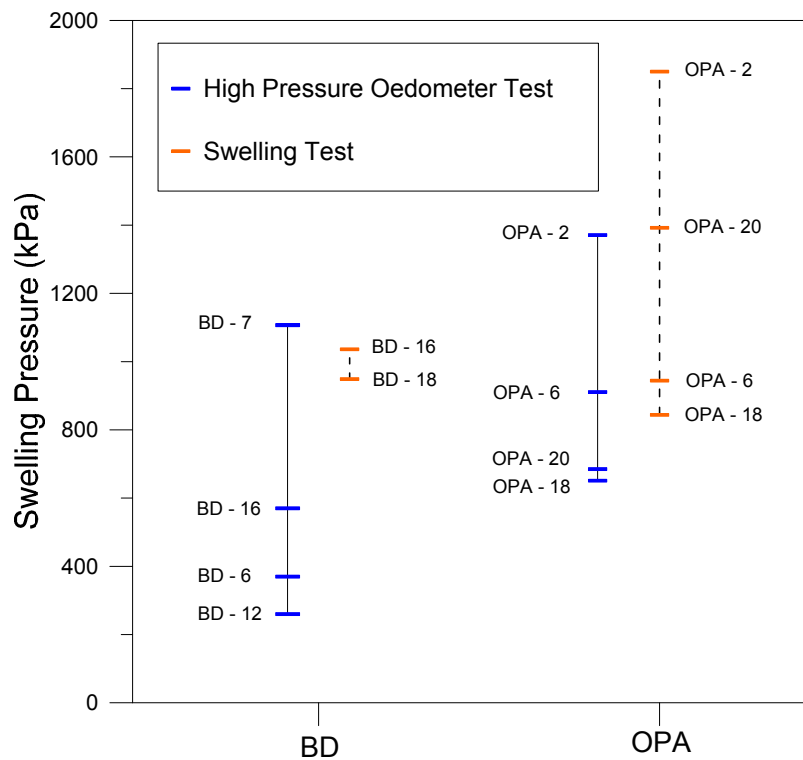


Fig. 5-13: Comparison of the values of swelling pressure obtained in the high pressure oedometer cell and with the constrained swelling tests.

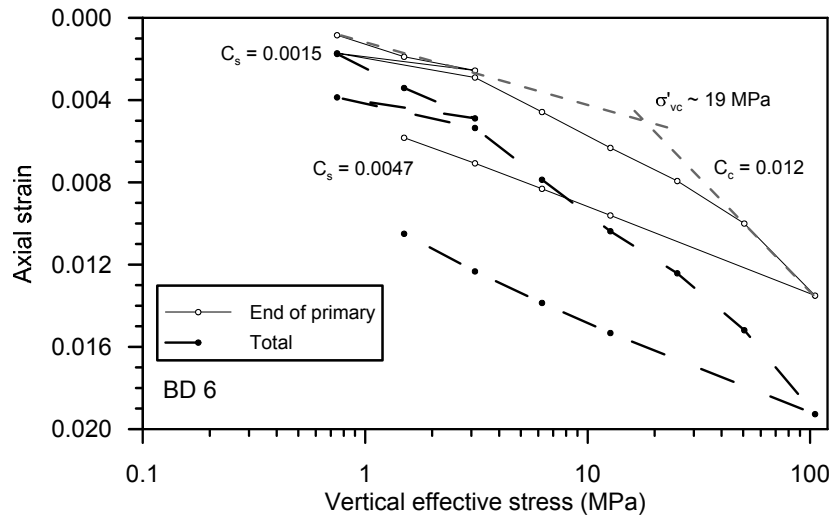


Fig. 5-14: Oedometric curve for the core BD-6.

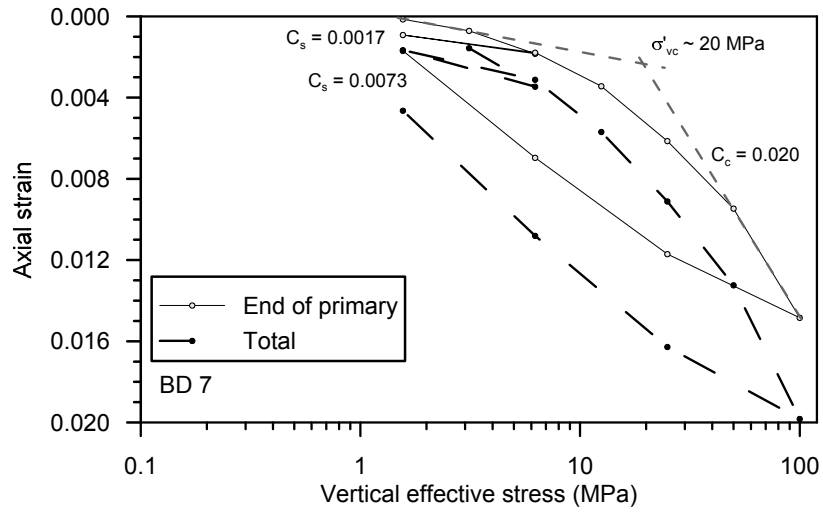


Fig. 5-15: Oedometric curve for the core BD-7.

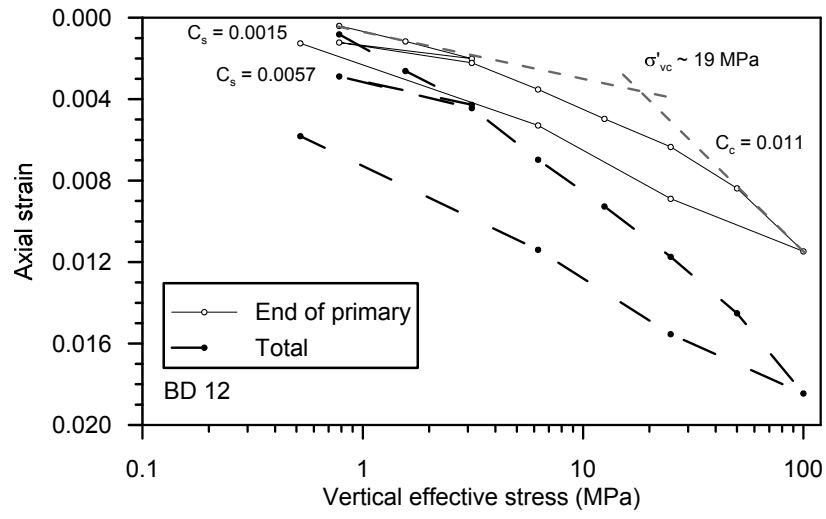


Fig. 5-16: Oedometric curve for the core BD-12.

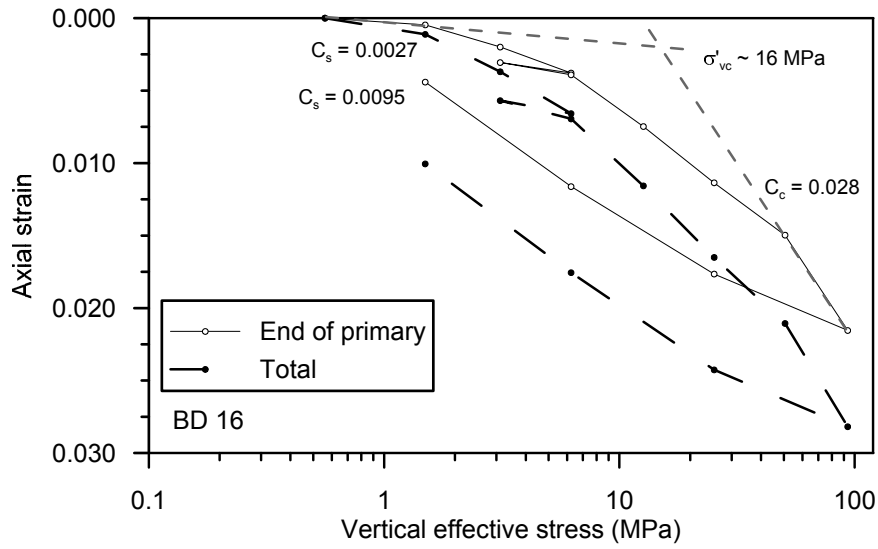


Fig. 5-17: Oedometric curve for the core BD-16.

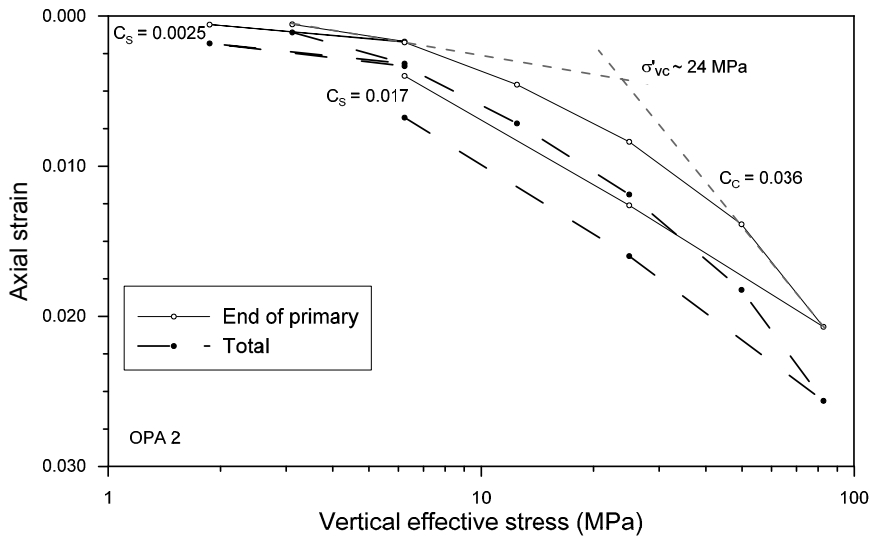


Fig. 5-18: Oedometric curve for the core OPA-2.

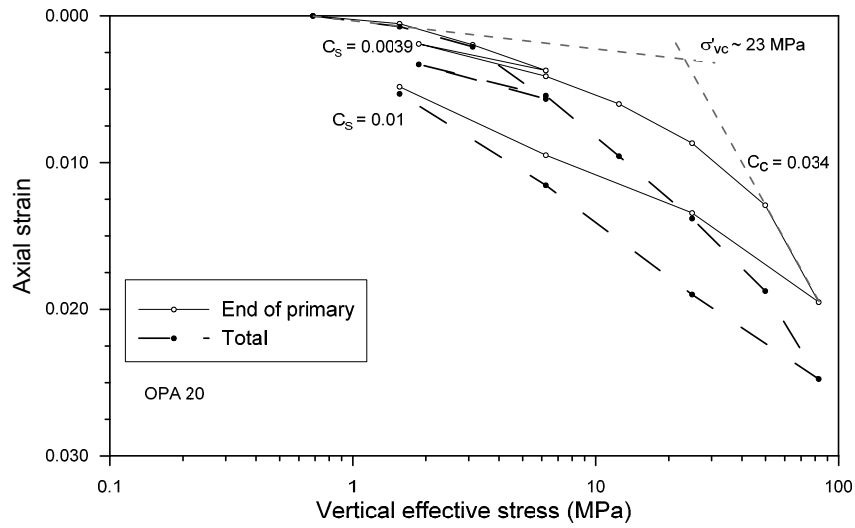


Fig. 5-19: Oedometric curve for the core OPA-20.

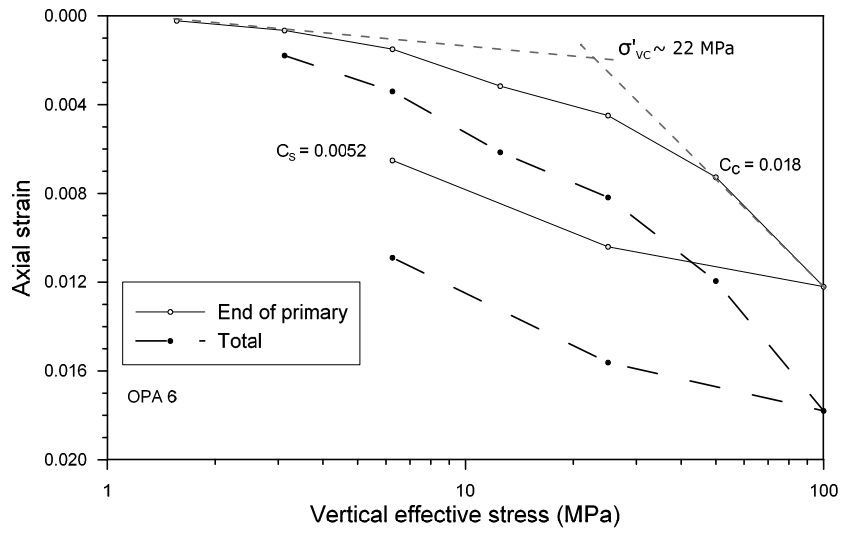


Fig. 5-20: Oedometric curve for the core OPA-6.

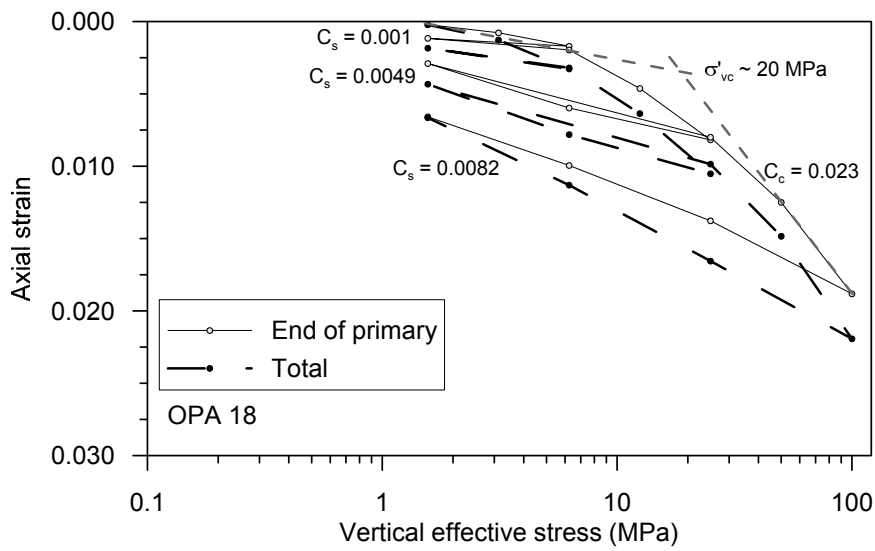


Fig. 5-21: Oedometric curve for the core OPA-18.

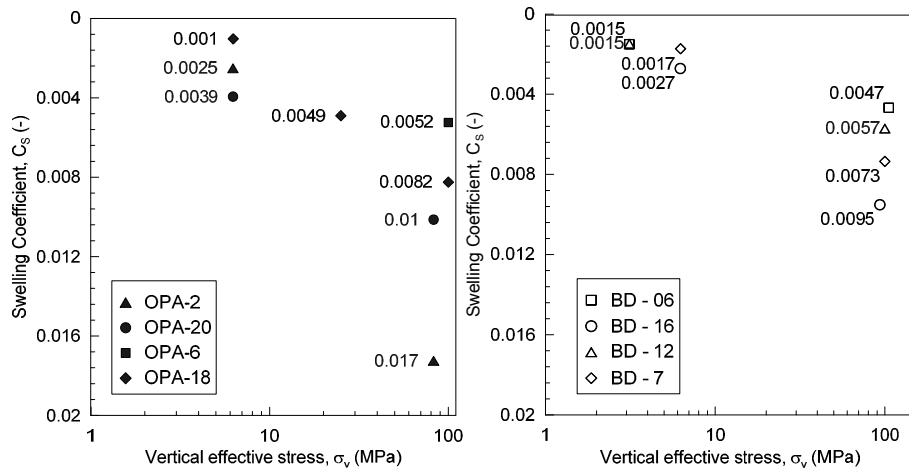


Fig. 5-22: Swelling coefficients versus maximum attained vertical effective stress for the 'Brown Dogger' and for the Opalinus Clay cores.

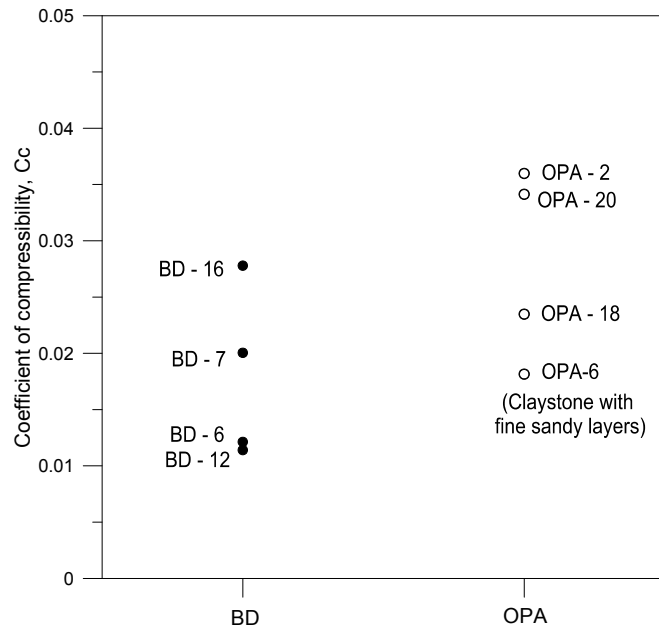


Fig. 5-23: Coefficients of compressibility for all the tested cores.

Tab. 5-5: Results of the high pressure oedometer tests: preconsolidation pressure, coefficient of compressibility and swelling coefficients for all the tested samples.

Core	σ'_{vc} [MPa]	C_c	C_s (~6MPa)	C_s (~25MPa)	C_s (~100MPa)
BD- 6	19	0.012	0.0015	-	0.0047
BD-16	20	0.020	0.0017	-	0.0073
BD-12	19	0.011	0.0015	-	0.0057
BD-7	16	0.028	0.0027	-	0.0095
OPA2	24	0.036	0.0025	-	0.0170
OPA20	23	0.034	0.0039	-	0.0100
OPA6	22	0.018	-	-	0.0052
OPA18	20	0.023	0.0010	0.0049	0.0082

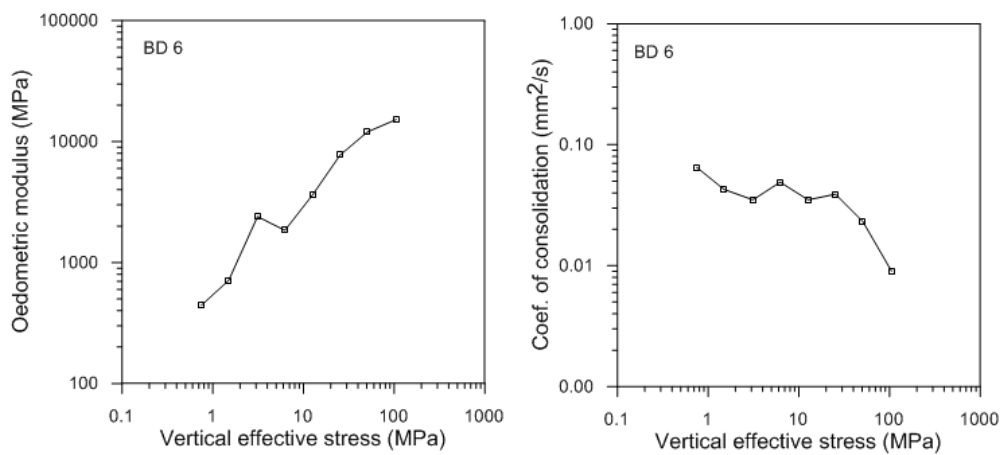


Fig- 5-24: Oedometric modulus and coefficient of consolidation versus vertical effective stress for core BD-6.

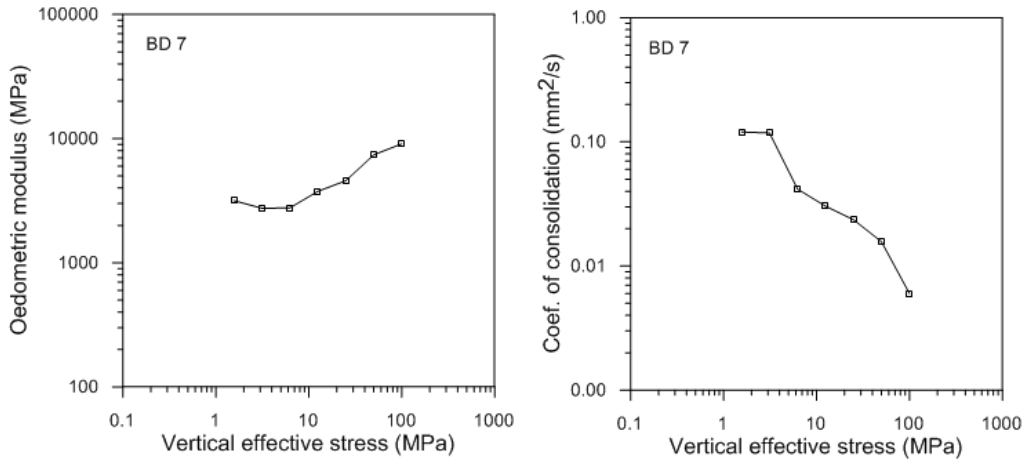


Fig- 5-25: Oedometric modulus and coefficient of consolidation versus vertical effective stress for the core BD-7.

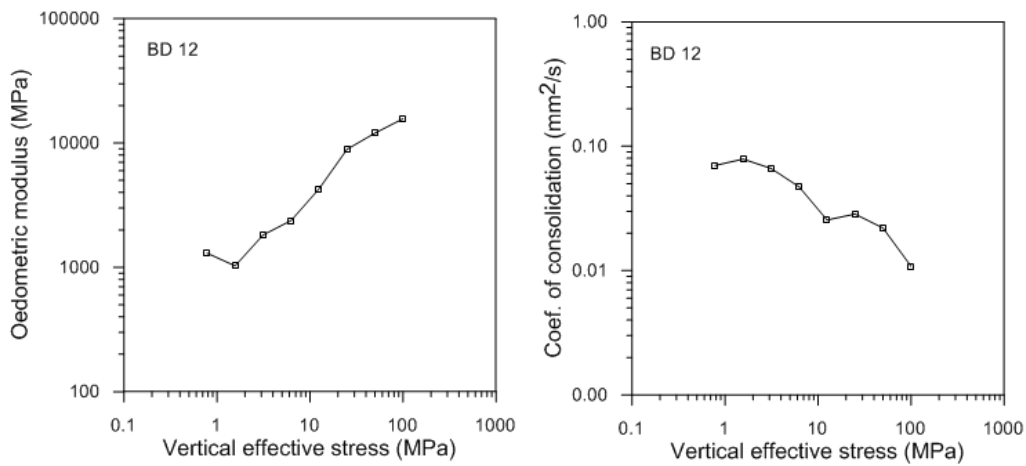


Fig 5-26: Oedometric modulus and coefficient of consolidation versus vertical effective stress for the core BD-12.

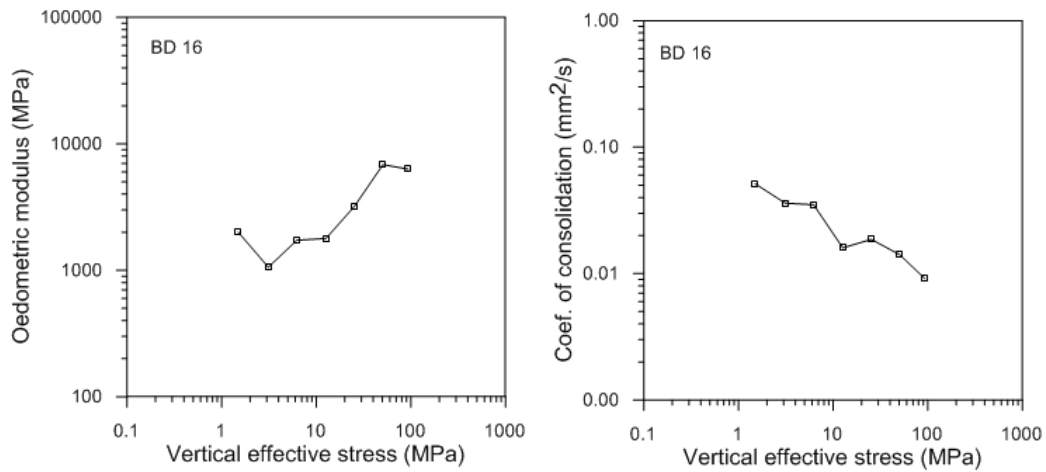


Fig. 5-27: Oedometric modulus and coefficient of consolidation versus vertical effective stress for the core BD-16.

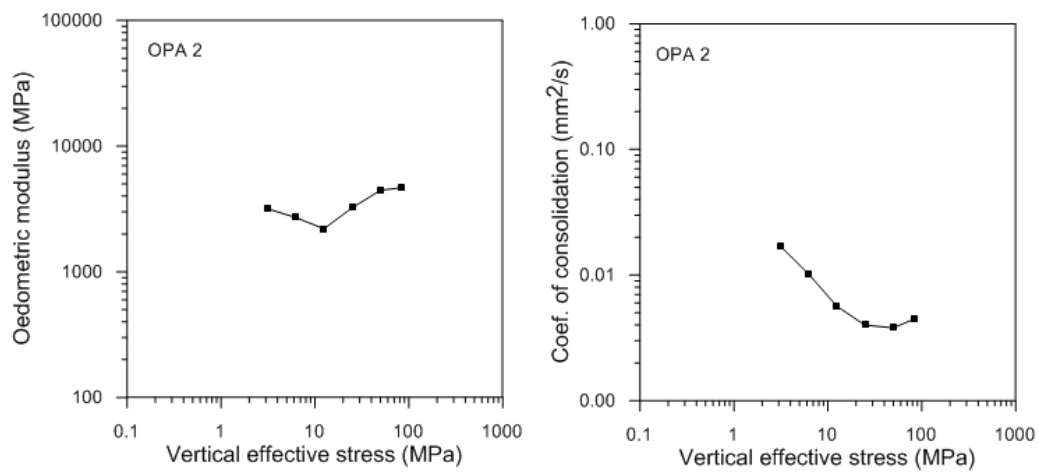


Fig. 5-28: Oedometric modulus and coefficient of consolidation versus vertical effective stress for the core OPA-2.

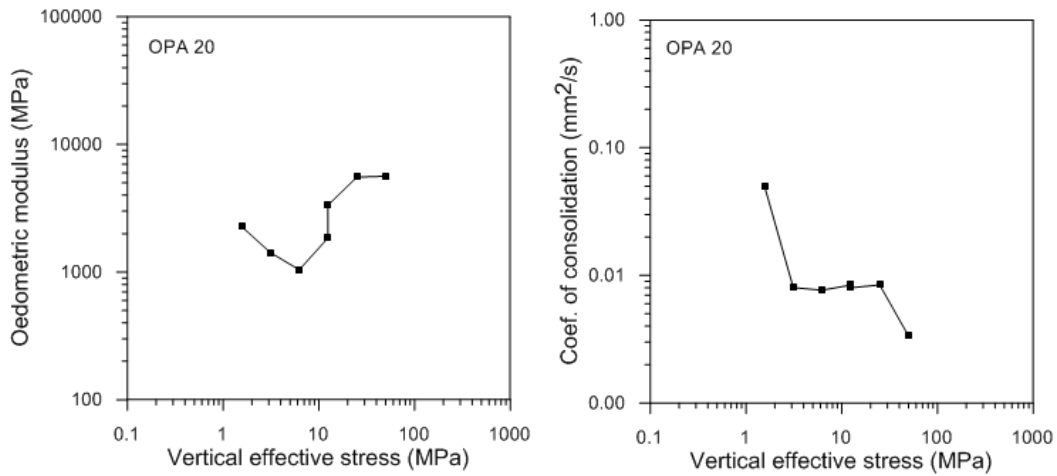


Fig. 5-29: Oedometric modulus and coefficient of consolidation versus vertical effective stress for the core OPA-20.

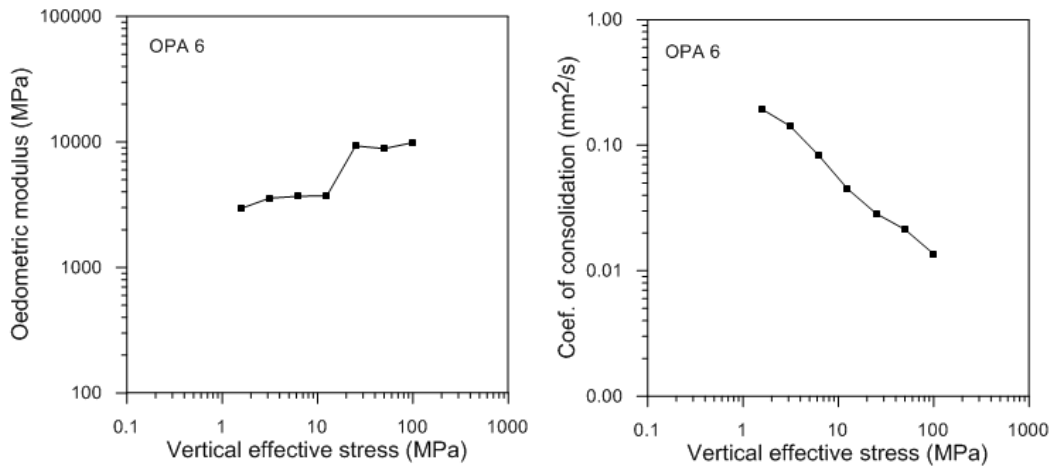


Fig. 5-30: Oedometric modulus and coefficient of consolidation versus vertical effective stress for the core OPA-6.

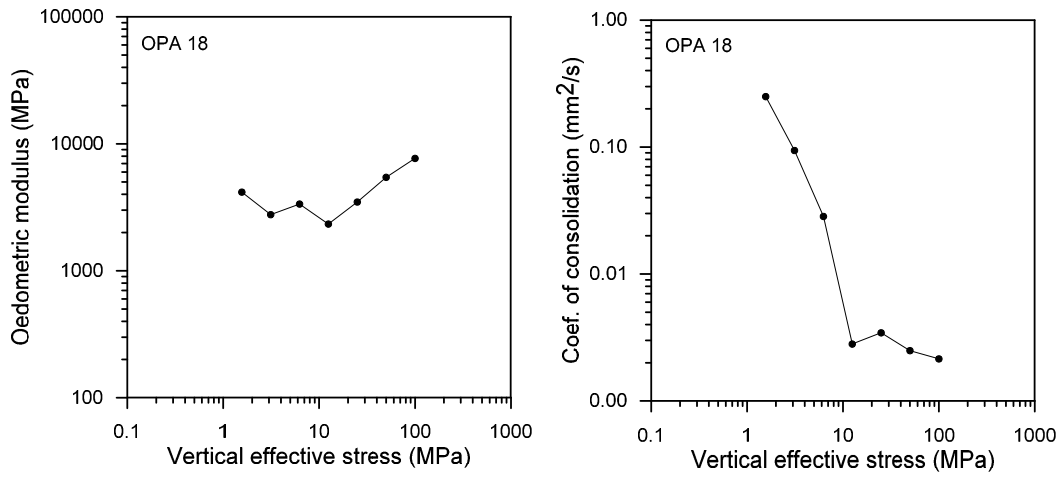


Fig 5-31: Oedometric modulus and coefficient of consolidation versus vertical effective stress for the core OPA-18.

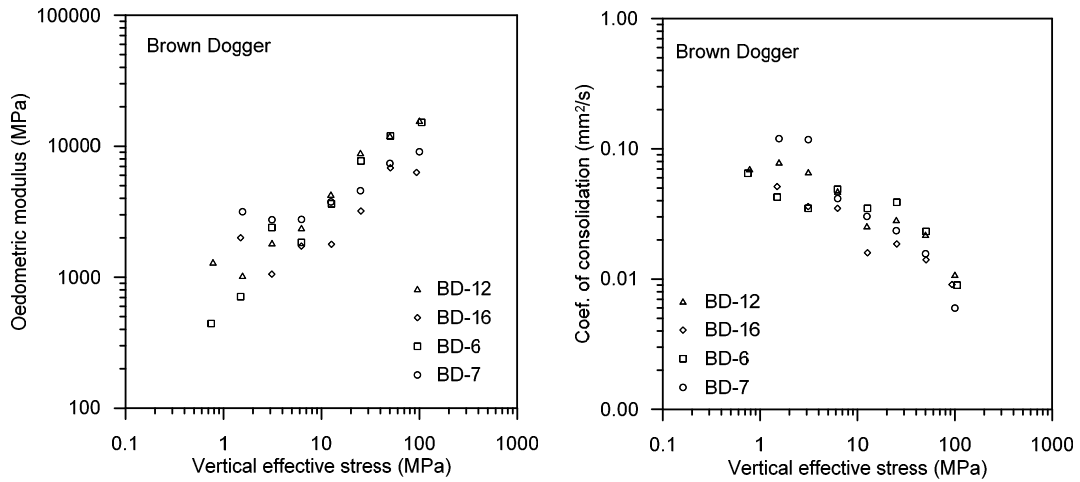


Fig 5-32: Oedometric modulus and coefficients of consolidation versus vertical effective stress for the 'Brown Dogger' cores.

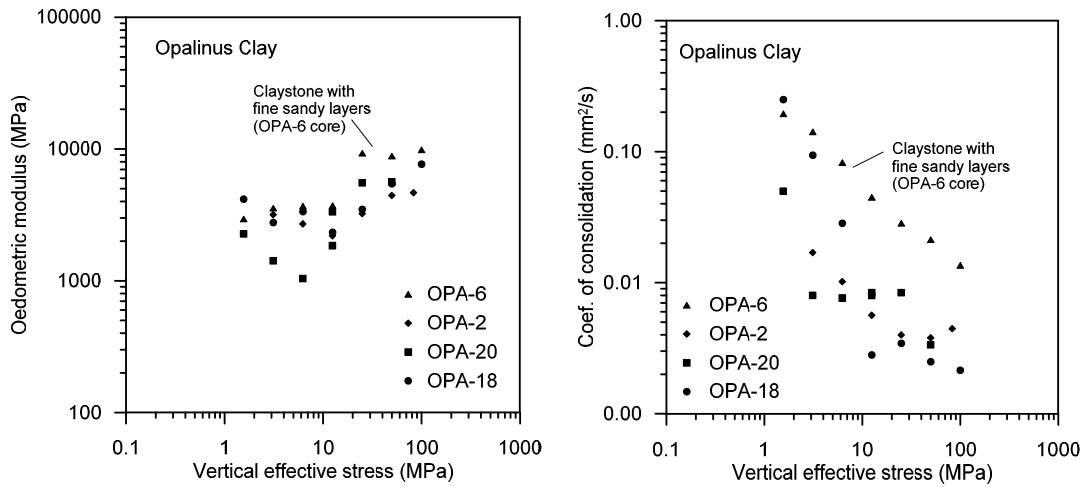


Fig. 5-33: Oedometric modulus and coefficients of consolidation versus vertical effective stress for the Opalinus Clay cores.

The intrinsic permeability (k) was calculated for all the cores at each loading step considering the following definition:

$$k = \frac{c_v \gamma_w}{E_{oed}} \tag{5-1}$$

where γ_w is the specific weight of water.

The results in terms of permeability versus vertical effective stress and void ratio for the cores from the 'Brown Dogger' formation and for the cores from the Opalinus Clay formation are plotted in Figure 5-34 and Figure 5-35. The observed values of permeability fall in the range of $10^{-12} - 10^{-14}$ m/s for both 'Brown Dogger' and Opalinus Clay (slightly lower values are observed for the Opalinus Clay); the greater permeability of OPA-6 compared to the other OPA cores can be justified with the presence of the fine-sandy layers. The comparison of the results for the two formations in terms of coefficient of permeability versus vertical effect stress and void ratio is shown in Figure 5-36.

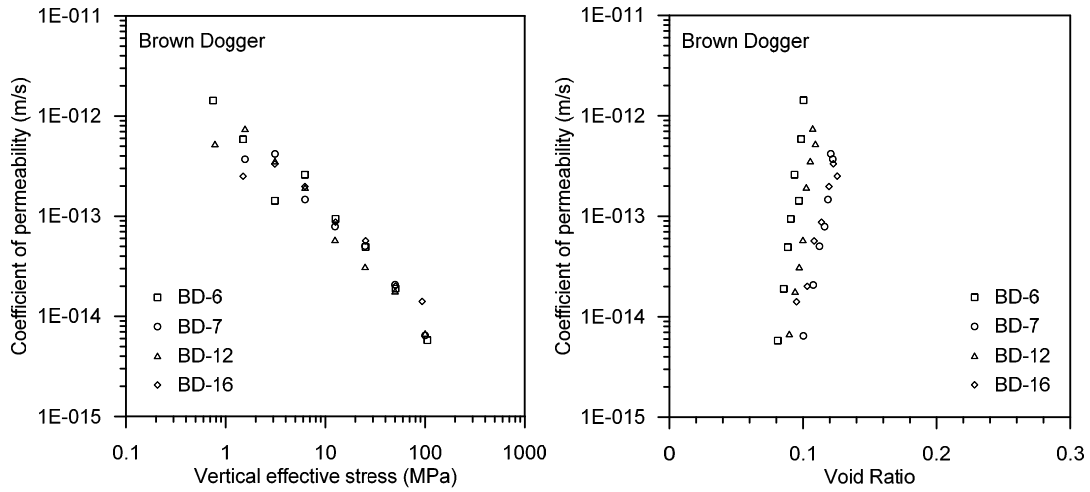


Fig. 5-34: Permeability versus vertical effective stress and permeability versus void ratio for the cores from the 'Brown Dogger' formation, as back-calculated from the analysis of the settlement versus time curves.

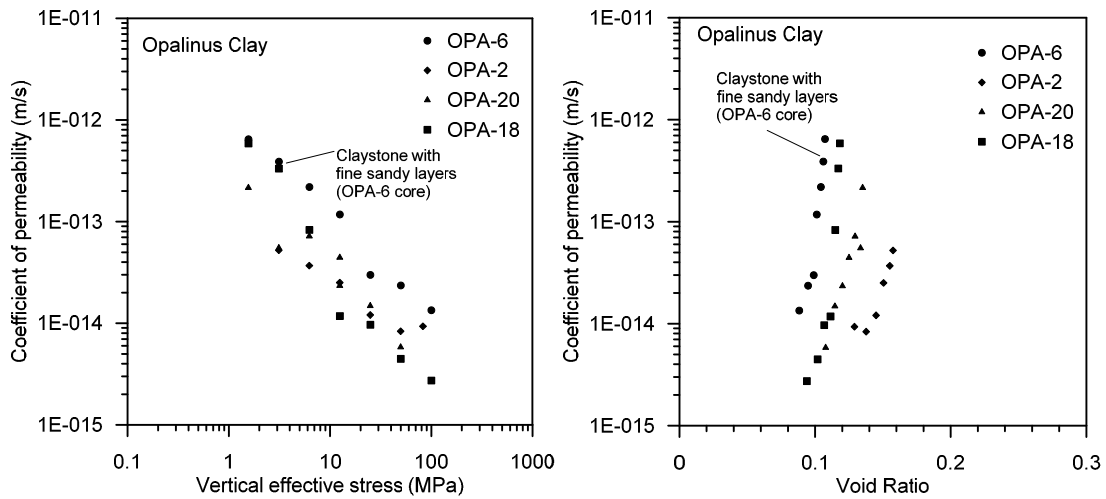


Fig. 5-35: Permeability versus vertical effective stress and permeability versus void ratio for the cores from the Opalinus Clay formation, as back-calculated from the analysis of the settlement versus time curves.

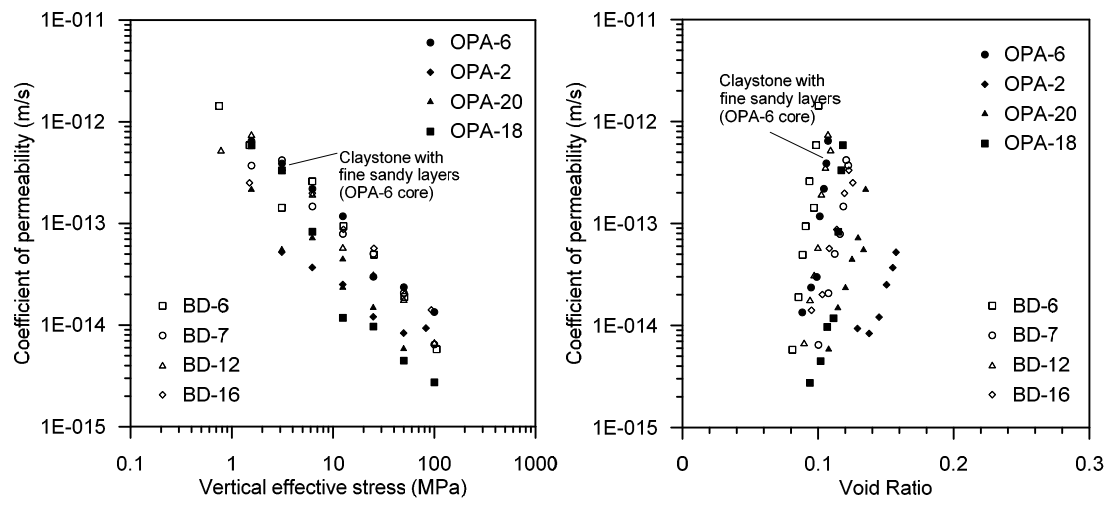


Fig. 5-36: Comparison of permeability versus vertical effective stress and permeability versus void ratio for the cores from the 'Brown Dogger' and Opalinus Clay formations.

6 Conclusions

This report presents the experimental activities carried out by the Laboratory for Soil Mechanics (LMS) of the Swiss Federal Institute of Technology in Lausanne (EPFL) on core samples extracted from a deep geothermal well near the village of Schlattigen in the Molasse Basin of Northern Switzerland. The test program is described in Section 2. Section 3 presents the results of the cores characterization in terms of index properties and pore size distribution. Section 4 describes the determination of the water retention curves. Mechanical tests are presented in Section 5.

A high-pressure oedometric cell was used to analyse the transition from the over- to the normally consolidated state of the shale samples. Vertical effective stresses in the range of 100 MPa had to be applied to measure the yield vertical stress. Analysis of the settlement versus time curves yielded information on the consolidation parameters and the permeability at various stress levels and void ratios.

The procedures adopted for the analyses of the water retention behaviour of shales consisted of controlling the water content by the addition of synthetic water or by the dehydration of the material in a desiccator; additionally, the procedure involved the measurement of total suction by a dew-point psychrometer. The method is suitable for measuring the water retention behaviour along the main drying and wetting paths and for highlighting the hysteretic behaviours of retention curve.

The analysis of the obtained results leads to the following conclusions:

- The grain size distribution curves highlight a slightly greater percentage of fine material in the Opalinus Clay compared to the 'Brown Dogger' formation. This observation is confirmed also by higher liquid limits for the Opalinus Clay.
- The evolution of the void ratio with suction shows a greater void ratio variation for the Opalinus Clay which presents a swelling of about 9 % at saturated conditions while about 6 % of swelling is observed for the 'Brown Dogger'. These results are in very good agreement with the free swelling tests results presented in Section 5. The conclusions that can be drawn so far are that the Opalinus Clay shale presents a greater swelling potential as well as a greater density of small pores. The MIP tests can help understanding the role of the solid phase structure on the retention properties; the results show a greater presence of smaller pores in the Opalinus Clay as well as a greater entrapped porosity (porosity that cannot be extruded). This observation might lead to lower values of hydraulic conductivity as it has been observed in the oedometer tests.
- The observations so far presented are confirmed by the results of the high pressure oedometric tests where greater values of swelling pressure at saturation are found for the Opalinus Clay. The analysis of the oedometric curves gives indication on the stress- strain behaviour of the material considered in this study. The development of greater axial strains for the Opalinus Clay shale compared to the 'Brown Dogger' is noticed, so that greater values of coefficient of compressibility are observed for the former compared to the latter.
- A systematic increase of the swelling coefficient with the preconsolidation pressure can be highlighted for all the material tested; this phenomenon could be explained by a loss of stiffness during the unloading phase due to the formation of micro-fractures as the stresses increase. In the end, the analysis of the high pressure oedometric tests results highlight lower values of coefficient of consolidation and permeability for the Opalinus Clay shale compared to the 'Brown Dogger' formation.

The analysis of the water retention behaviour of the material as well as the stress-strain behaviour is relevant not only for a clear determination of the shale properties, but also to get insight in the actual characteristics of the material at in situ conditions, when the boundary conditions are much more complex than those created in the research laboratory. In situ, the degree of complexity is mainly due to the coupled hydro-mechanical phenomena; indeed, the material may undergo desiccation (or saturation) which causes changes in the effective stress. The changes in effective stress determine changes in the porosity and effective permeability which, in turn, affect the capillary forces between the soil particles, thus affecting the retention properties of the material.

The analysis carried on in this experimental program was mainly devoted to the understanding of the shale behaviour considering decoupled conditions (retention behaviour under unstressed conditions and analysis of the stress/strain behaviour of the material under saturated condition). Coupling the results of the analysis is necessary in order to evaluate the real properties (porosity, effective permeability) and behaviour (stress-strain) of the material under in situ conditions.

It is important to state that the characteristics of the core samples that are used for the experimental investigations in the research laboratory are different from the in situ characteristics, this is due to the fact that the stresses were released during the coring process and the material may have experienced desiccation as a consequence of the exposure to atmosphere before preservation. Both processes may have influenced the properties of the cores, causing an increase in porosity (due to the stress release) but also the development of negative water pressure (suction) which may affect the relation between stress and strain. The mentioned relationship has been well interpreted by the analysis of the results of the high pressure oedometric tests but, as anticipated, this cannot be considered as the real behaviour of the material since during the release of the stresses it experiences also changes in the degree of saturation and porosity due to desiccation processes.

The previous considerations are useful in order to deduce the in situ properties of the material from the results of the laboratory investigation. Once the suction values of the core samples are measured, it is possible to deduce the value of porosity at saturated conditions from the analysis of the water retention behaviour. As it was observed in Section 4.2.1, the porosity changes are more significant for the lowest range of suction variations; nevertheless the great changes of porosity to reach the saturation from the initial conditions of the core samples, can be linked to the fact that the material is unstressed and the volume changes (swelling/shrinkage) are allowed. The different in situ conditions may lead to suction changes when the material is still under great mechanical stresses. As consequence, the change in porosity cannot be evaluated only from the water retention curves but the coupling with results of the stress/strain behaviour analysis is necessary.

The water retention curves allow deriving, from the core conditions in laboratory, the value of porosity of the saturated material under unstressed conditions; this value is surely higher than the in situ value due to the high in situ stresses which reduce the porosity and the effective permeability. The value of void ratio estimated from the analysis of the water retention behaviour can be considered as the upper limit of the porosity range of the in situ material. The positive variation of porosity is reduced considering the stress increase when the sample is brought to the in situ stress conditions (through the high pressure oedometric test) which cause a negative variation (decrease) of porosity.

The high pressure oedometric test is carried out under saturated conditions, so the negative variation (decrease) of porosity with increasing effective stress that is observed is the maximum

negative variation that can be observed since an increase of suction values would lead to increasing capillary forces and stiffness of the material thus increasing the elastic domain and reducing the porosity variation along the re-loading path.

Summarizing the above experimental evidence, the following statements can be made: at fully saturated (in-situ) conditions it can be assumed that porosity increased due to swelling phenomena. On the other hand, at high total stress (i.e. at great depth) porosity will decrease due to the increase of effective stress. The two mentioned processes are not decoupled, they develop together, influencing each other, thus a coupled investigation should be considered in order to clearly understand how these phenomena interact.

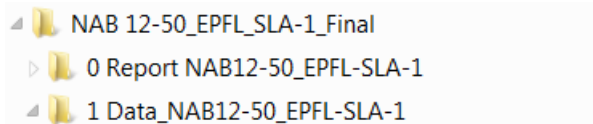
7 References

- Albert, W., H.R. Bläsi, H. Madritsch, T. Vogt, H.P. Weber (2012): Geologie, Stratigraphie, Strukturgeologie, bohrlochgeophysikalisches Logging und Wasserproben der Geothermiebohrung Schlattingen SLA-1 (Rohdaten). Nagra Project Report NPB 12-16, Nagra, Wettingen, Switzerland.
- Cardoso, R., Romero, E., Lima, A. & Ferrari, A. (2007). A comparative study of soil suction measurement using two different high-range psychrometers. In: Schanz, T. (Ed.) 2nd Int. Conf. on Mech. of Unsat. Soils, Weimar (Germany). Springer-Verlag Berlin (Germany), pp. 79-93.
- Ferrari A. and Laloui L. Advances in the testing of the hydro-mechanical behaviour of shales. In L. Laloui and A. Ferrari editors. *Multiphysical Testing of Soils and Shales*, pages 57-68, Springer, 2012.
- Holzer, L., Münch, B., Rizzi, M., Wepf, R., Marschall, P., Graule, T. (2010): 3D-microstructure analysis of hydrated bentonite with cryo-stabilized pore water. *Applied clay science* 47, 330-342.
- Huertas F., Fuentes-Cantillana J.L., Julien F., Rivas P., Linares J., Fariña P., Ghoreychi M., Jockwer N., Kickmaier W., Martinez M.A., Samper J., Alonso E. and Elorza F.J., 2000. "Full-scale engineered barriers experiment for a deep geological repository for high-level radioactive waste in crystalline host rock (FEBEX project)" European Commission EUR 19147. Luxembourg.
- Leong, E.-C., Tripathy, S. & Rahardjo, H. (2003). Total suction measurement of unsaturated soils with a device using the chilled-mirror dew point technique. *Géotechnique*, Vol. 53, No. 2, pp. 173-182.
- Peron, H., Hueckel, T., & Laloui, L. "An improved volume measurement for determining soil water retention curves", *Geotechnical Testing Journal*, vol. 30 no. 1:1 – 8, 2007.
- Salager S., Ferrari A. and Laloui L. New experimental tools for the characterization of highly overconsolidated clayey materials in unsaturated conditions. In L. Laloui, editor, *Mechanics of unsaturated geomaterials*, pages 113-126. John Wiley & sons, 2010.
- Traber, D. (2011). Recipe and preparation of a simplified artificial pore water for Opalinus Clay and 'Brown Dogger' (personal communication / internal memo).
- Van Genuchten, M. Th. (1980). A closed-form equation for predicting the hydraulic conductivity of unsaturated soils. *Soil Sci. Soc. Am. J.*, 44, 892–898.

Appendix A – Structure of the electronic data base

Overview

Auxiliary digital files containing the whole set of data were made available to NAGRA. The electronic data base ensures the traceability of the reported raw data and the results of data analyses and collects all graphical data representations. The electronic data base is organized in the 2 main directories:



The detailed description of the contents of the directory "1 Data NAB12-50_EPFL-SLA-1"



The data directory "1 Data NAB12-50_EPFL-SLA-1"

The data directory contains all raw data and data interpretations according to the sequence of the report outline (HPO, Identification, MIP, RC, Swelling, Mineralogy). The sub-directory "HPO" comprises the EXCEL Files with the oedometer tests:

BD6_HPO_interpretation.xlsx	16.11.2012 10:23	Microsoft Excel-Ar...	36 KB
BD7_HPO_interpretation.xlsx	16.11.2012 10:23	Microsoft Excel-Ar...	34 KB
BD12_HPO_interpretation.xlsx	16.11.2012 10:27	Microsoft Excel-Ar...	35 KB
BD16_HPO_interpretation.xlsx	16.11.2012 10:26	Microsoft Excel-Ar...	34 KB
OPA2_HPO_interpretation.xlsx	16.11.2012 10:26	Microsoft Excel-Ar...	33 KB
OPA6_HPO_interpretation.xlsx	16.11.2012 10:25	Microsoft Excel-Ar...	33 KB
Opa18_HPO_interpretation.xlsx	16.11.2012 10:25	Microsoft Excel-Ar...	42 KB
OPA20_HPO_interpretation.xlsx	16.11.2012 10:25	Microsoft Excel-Ar...	33 KB

The sub-directory "Identification" comprises the EXCEL Files with the identification tests:

geotech_classification_nov2012.xlsx	06.11.2012 16:05	Microsoft Excel-Ar...	162 KB
grain_size_summary.xlsx	01.10.2012 18:31	Microsoft Excel-Ar...	41 KB

The sub-directory "MIP" comprises the EXCEL Files with the mercury intrusion tests:

	MIP_inerpretations_BD-7.xls	05.11.2012 16:50	Microsoft Excel 97...	863 KB
	MIP_inerpretations_BD-16.xls	05.11.2012 17:51	Microsoft Excel 97...	502 KB
	MIP_inerpretations_BD-30.xls	05.11.2012 17:52	Microsoft Excel 97...	717 KB
	MIP_inerpretations_EFM-1.xls	05.11.2012 17:52	Microsoft Excel 97...	666 KB
	MIP_inerpretations_OPA3.xls	05.11.2012 17:53	Microsoft Excel 97...	708 KB
	MIP_interpretation_BD6.xls	05.11.2012 17:53	Microsoft Excel 97...	655 KB

The sub-directory "RC" comprises the EXCEL Files with the water retention tests:

	WRC - BD7- W_only.xlsx	05.11.2012 17:08	Microsoft Excel-Ar...	43 KB
	WRC - BD18 - drying only.xlsx	05.11.2012 17:08	Microsoft Excel-Ar...	33 KB
	WRC - BD30.xlsx	06.11.2012 14:36	Microsoft Excel-Ar...	36 KB
	WRC - EFM1.xlsx	05.11.2012 16:53	Microsoft Excel-Ar...	23 KB
	WRC - OPA6.xlsx	05.11.2012 17:08	Microsoft Excel-Ar...	62 KB
	WRC - OPA18.xlsx	05.11.2012 17:07	Microsoft Excel-Ar...	47 KB
	WRC - OPA20.xlsx	05.11.2012 17:08	Microsoft Excel-Ar...	52 KB
	Water Retention Curve_BD6.xlsx	05.11.2012 17:31	Microsoft Excel-Ar...	75 KB
	Water retention curve_BD12.xlsx	05.11.2012 17:14	Microsoft Excel-Ar...	42 KB
	Water retention curve_BD18.xlsx	05.11.2012 17:17	Microsoft Excel-Ar...	35 KB
	WRC - OPA3 - kerdane.xlsx	05.11.2012 17:17	Microsoft Excel-Ar...	51 KB

The sub-directory "Swelling" comprises the EXCEL Files with the swelling tests:

	Constrained_swelling_BD-16.xls	05.11.2012 11:11	Microsoft Excel 97...	2'435 KB
	Constrained_swelling_BD-18.xls	05.11.2012 11:14	Microsoft Excel 97...	354 KB
	Constrained_swelling_OPA-2.xls	05.11.2012 11:15	Microsoft Excel 97...	487 KB
	Constrained_swelling_OPA-6.xls	05.11.2012 11:24	Microsoft Excel 97...	297 KB
	Constrained_swelling_OPA-18.xls	05.11.2012 11:29	Microsoft Excel 97...	386 KB
	Constrained_swelling_OPA-20.xls	05.11.2012 11:27	Microsoft Excel 97...	565 KB
	Free_swelling_BD-18.xls	05.11.2012 11:29	Microsoft Excel 97...	761 KB
	Free_swelling_OPA-20.xls	05.11.2012 11:30	Microsoft Excel 97...	121 KB

The sub-directory "Mineralogy" comprises the EXCEL Files with the mineralogical analyses:

	Mineralogy NAB 12-50_1.13.xls	22.01.2013 11:06	Microsoft Excel 97...	35 KB
---	-------------------------------	------------------	-----------------------	-------

Appendix B – Mineralogical Analyses of the Core samples by Professor Martin Mazurek / University of Berne

Lithology	NAGRA Code	Sample ID	Depth [m]	Quartz [wt.%]	K-feldspar [wt.%]	Albite [wt.%]	Calcite, corr. [wt.%]	Dolomite / Ankerite corr. [wt.%]	Siderite corr. [wt.%]	Pyrite [wt.%]	C(org) [wt.%]	Sheet silicates [wt.%]
Clay to Argillaceous Marl	BD-6	SLA	766.84	21	2.0	<1	51	0.0	<1	0.9	<0.1	25
Clay to Argillaceous Marl	BD-16	SLA	769.70	15	3.0	<1	53	2.8	<1	1.1	<0.1	25
Clay to Argillaceous Marl	BD-18	SLA	775.06	20	3.0	<1	26	1.5	<1	2.1	0.1	47
Argillaceous Marl	BD-12	SLA	778.41	11	2.0	<1	55	2.6	<1	0.9	<0.1	28
Calcareous Marl	BD-7	SLA	781.33	18	3.0	<1	29	4.4	<1	1.7	0.1	43
Calcareous Marl	BD-30	SLA	807.29	32	4.0	1.0	38	1.3	<1	1.1	<0.1	23
Clay to Argillaceous Marlstone	OPA-3	SLA	837.55	17	2.0	<1	16	<1	1.0	0.7	0.4	63
Claystone	OPA-2	SLA	838.12	17	2.0	<1	11	<1	<1	1.9	0.4	68
Claystone	OPA-20	SLA	854.71	32	4.0	1.0	14	2.1	0.9	0.7	0.3	44
Claystone with fine-sandy layers (ca. 1 mm)	OPA-6	SLA	882.35	25	2.0	<1	21	<1	1.8	0.4	0.1	50
Claystone with sandy layers	OPA-18	SLA	891.13	28	3.0	<1	15	1.9	1.4	0.9	0.1	50

Data file enclosed in Appendix A.